Global Warming and the Weakening of the Tropical Circulation

GABRIEL A. VECCHI

NOAA/Geophysical Fluid Dynamics Laboratory, Princeton, New Jersey

BRIAN J. SODEN

Rosenstiel School for Marine and Atmospheric Science, University of Miami, Miami, Florida

(Manuscript received 23 August 2006, in final form 20 December 2006)

ABSTRACT

This study examines the response of the tropical atmospheric and oceanic circulation to increasing greenhouse gases using a coordinated set of twenty-first-century climate model experiments performed for the Intergovernmental Panel on Climate Change (IPCC) Fourth Assessment Report (AR4). The strength of the atmospheric overturning circulation decreases as the climate warms in all IPCC AR4 models, in a manner consistent with the thermodynamic scaling arguments of Held and Soden. The weakening occurs preferentially in the zonally asymmetric (i.e., Walker) rather than zonal-mean (i.e., Hadley) component of the tropical circulation and is shown to induce substantial changes to the thermal structure and circulation of the tropical oceans. Evidence suggests that the overall circulation weakens by decreasing the frequency of strong updrafts and increasing the frequency of weak updrafts, although the robustness of this behavior across all models cannot be confirmed because of the lack of data. As the climate warms, changes in both the atmospheric and ocean circulation over the tropical Pacific Ocean resemble "El Niño–like" conditions; however, the mechanisms are shown to be distinct from those of El Niño and are reproduced in both mixed layer and full ocean dynamics coupled climate models. The character of the Indian Ocean response to global warming resembles that of Indian Ocean dipole mode events. The consensus of model results presented here is also consistent with recently detected changes in sea level pressure since the mid–nineteenth century.

1. Introduction

Throughout much of the discussion of global warming, it is often assumed that atmospheric convection will increase as the climate warms. For example, Lindzen (1990) argued that tropical convection would increase in a warmer climate because of the destabilizing effects of increased lower-tropospheric moisture. Betts and Ridgway (1989)—see also Betts (1998)—were the first to suggest that convection might actually decrease in a warmer climate, based upon an analysis of the boundary layer equilibrium response to increasing SSTs. Using a one-dimensional radiative convective model, they showed that the rate of moisture increase in the boundary layer, under the assumption of constant relative humidity, outpaced the rate of increase in evaporation and thus necessitated a decrease in the convective mass circulation in the Tropics. A study using coupled ocean–atmospheric models also suggested that the convection might decrease in a warmer climate noting that the dry static stability increases at a faster rate than the radiative cooling of the troposphere thus implying a weakening of the subsidence rate (Knutson and Manabe 1995). Held and Soden (2006) suggested that the slowing of the atmospheric overturning circulation in response to global warming could be understood through the differential response of global-mean precipitation and atmospheric humidity to a warming climate.

Some modes of tropical climate variability are fundamentally tied to interactions between the ocean and atmosphere: for example, the El Niño–Southern Oscillation (ENSO) phenomenon (e.g., Wyrtki 1975; Zebiak

Corresponding author address: Dr. Gabriel A. Vecchi, NOAA/Geophysical Fluid Dyamics Laboratory, Forrestal Campus, Princeton, NJ 08542.
E-mail: Gabriel.A.Vecchi@noaa.gov

DOI: 10.1175/JCLI4258.1

TABLE 1. IPCC AR4 models from which scenario A1B data are available and were used in this analysis. An asterisk indicates that oceanic vertical velocity was not available. Atmospheric vertical velocity data were not available from BCCR BCM2.0, CSIRO Mk3.0, and MIUB-ECHO-G.

Model name	Country	Oceanic resolution	Atmospheric resolution	Reference	Ocean data	Slab
1 BCCR BCM2.0	Norway	2.4° × 2.4° (0.8°) σ24	T63 L31	Furevik et al. (2003)	Yes*	
2 CGCM3.1 T47	Canada	1.85° × 1.85° L29	T47 L31	Kim et al. (2002)	Yes	
3 CGCM3.1 T63	Canada	1.4° × 0.94° L29	T63 L31	Kim et al. (2002)	Yes	
4 CNRM CM3	France	2° × 0.5° L31	T63 L45	Salas y Mélia et al. (2006)	Yes	
5 CSIRO Mk3.0	Australia	1.875° × 0.84° L31	T63 L18	Gordon et al. (2002)	Yes*	
6 GFDL CM2.0	United States	1° × 1° (1/3°) L50	2.5° × 2° L24	Delworth et al. (2006)	Yes	Yes
7 GFDL CM2.1	United States	1° × 1° (1/3°) L50	2.5° × 2° L24	Delworth et al. (2006)	Yes	Yes
8 GISS AOM	United States	4° × 3 L16	4° × 3° L12	Lucarini and Russell (2002)	Yes	
9 GISS-EH	United States	2° × 2° L16	5° × 4° L20	Schmidt et al. (2006)	Yes	
10 GISS-ER	United States	5° × 4° L13	5° × 4° L20	Schmidt et al. (2006)	Yes	Yes
11 IAP FGOALS	China	1° × 1° L33	T42 L26	Yu et al. (2004)	Yes	
12 INM CM3.0	Russia	2.5° × 2° L33	5° × 4° L21	Volodin and Diansky (2004)	Yes	Yes
13 IPSL CM4	France	2° × 1° L31	2.5° × 3.75° L19	Marti et al. (2005)	Yes	
14 MIROC Hi	Japan	0.28° × 0.19° L47	T106 L56	Hasumi and Emori (2004)	Yes*	Yes
15 MIROC Med	Japan	1.4° × 0.5° L43	T42 L20	Hasumi and Emori (2004)	Yes	Yes
16 MIUB ECHO-G	Germany/Korea	2.8° × 2.8° L20	T30 L19	Min et al. (2005)	Yes	
17 MPI ECHAM5	Germany	1.5° × 1.5° L40	T63 L31	Jungclaus et al. (2006)		Yes
18 MRI CGCM2.3	Japan	2.5° × 0.5° L23	T42 L30	Yukimoto and Noda (2002)	Yes	Yes
19 NCAR CCSM3	United States	1.1° × 1.1° (0.27) L40	T85 L26	Collins et al. (2006)	Yes	Yes
20 NCAR PCM1	United States	2/3° × 1/2° L32	T42 L18	Washington et al. (2000)		
21 UKMet HadCM3	United Kingdom	1.25° × 1.25° L30	3.75° × 2.5° L19	Gordon et al. (2000)	Yes*	
22 UKMet HadGem1	United Kingdom	1° × 1° (1/3°) L40	1.875° × 1.25° L38	Johns et al. (2004)		Yes

and Cane 1987; Jin 1997; Wang and Picaut 2004) and the Indian Ocean dipole–zonal mode (IODZM; e.g., Saji et al. 1999; Webster et al. 1999; Yamagata et al. 2004). It has been suggested that ocean–atmosphere interactions of similar character to those of ENSO play a fundamental role in the tropical response to increased atmospheric CO_2, and could act to moderate global warming (Clement et al. 1996; Cane et al. 1997).

We use the archive of coupled climate models results organized by the Program for Climate Model Diagnosis and Intercomparison (PCMDI) for the Intergovernmental Panel on Climate Change (IPCC) Fourth Assessment Report (AR4) to assess the robustness of the atmospheric circulation response. We explore climate change simulations from 22 different coupled climate models integrated with projected changes in well-mixed greenhouse gases and aerosols as prescribed by the IPCC Special Report on Emissions Scenarios (SRES) A1B scenario. This scenario corresponds roughly to a doubling in equivalent CO_2 between 2000 and 2100, after which time the radiative forcings are held constant with some of the model integrations continuing for another 100–200 yr. To assess the impacts of dynamical ocean changes on the slowdown of atmospheric circulation, we also make use of output from the "slab" mixed layer ocean coupled model runs. The slab runs are a couplet of a control and a 2 × CO_2 perturbation experiment, in which the implicit ocean dynamics are not allowed to change. Table 1 summarizes the models used here; for each of the models we use only one ensemble member.[1]

We show that all the IPCC AR4 models project a weakening of the atmospheric overturning circulation as the climate warms, and this weakening is driven by changes in the atmospheric hydrologic cycle (e.g., Held and Soden 2006). The weakening is primarily manifest as a reduction in the zonally asymmetric overturning of air (i.e., the Walker circulation) rather than in the zonal-mean overturning (i.e., the Hadley circulation). The projected weakening is also captured in mixed layer climate model simulations, indicating that ocean dynamics are not critical to this response. However, the atmospheric slowdown does impact the thermodynamic and dynamic structure of the tropical oceans. As the formulations used to parameterize convection vary widely among these models, we argue that the consistency of the circulation response does not reflect a convergence of the representation of convective parameterizations. Rather, we show that the weakening of the circulation is consistent with simple thermodynamic

[1] Usually "run1," except for NCAR-PCM1 where we use "run2" because it is a 300-yr integration.

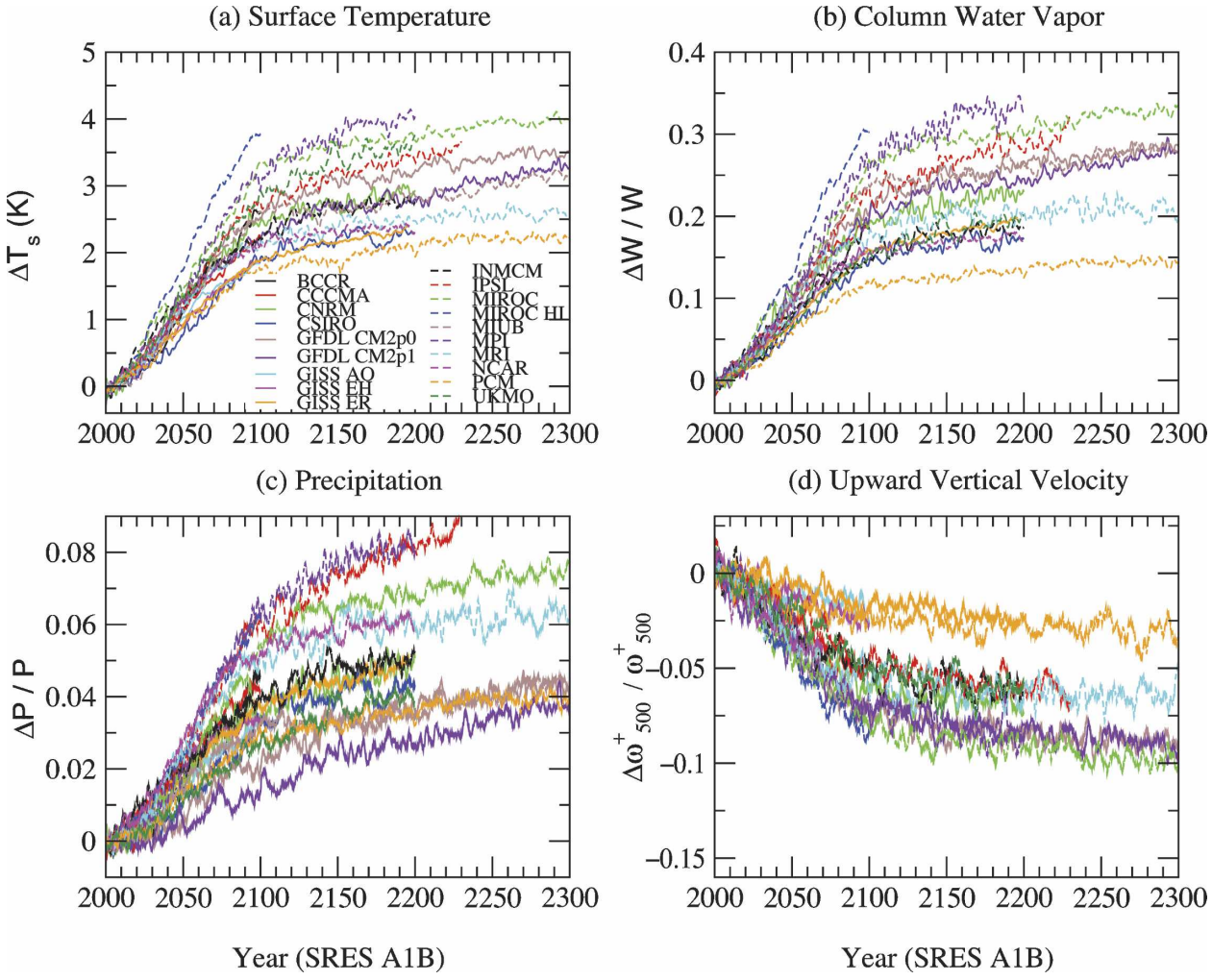

FIG. 1. Time series of the global-mean response of (a) surface air temperatures, (b) total column water vapor, (c) precipitation, and (d) upward component of the monthly mean vertical velocity at 500 hPa. The latter three quantities are expressed as the fractional change relative to the first 10 yr of the A1B integration (2000–10). All fields are computed by subtracting the mean seasonal cycle from 2000–10, global averaging, and then differencing the anomalies relative to their average computed over the first 10 yr of the simulation (2000–10).

and energetic arguments that constrain the global-scale response and support the behavior proposed by Betts and Ridgway (1989), Knutson and Manabe (1995), Betts (1998), Held and Soden (2006), and others.

2. Atmospheric response

Some aspects of climatic response to increased CO_2 are consistent across the IPCC AR4 models. Of particular relevance to our study is the global-mean response to increased CO_2 of four such quantities (Fig. 1): surface air temperatures (increase), total column water vapor (increase), precipitation (increase), and upward component of the monthly mean 500-hPa vertical velocity[2] (decrease). The results described in sections 2a and 2b revisit and build on the analysis of Held and Soden (2006), to which the reader is referred for a more comprehensive discussion.

a. Temperature and water vapor

All models show an increase in surface air temperature ranging from roughly 2–4 K by year 2200 (forcing changes remain constant after year 2100). The total col-

[2] Upward atmospheric vertical velocity at 500 hPa is computed by integrating the monthly mean pressure velocity over all model grid points that have ascending motion.

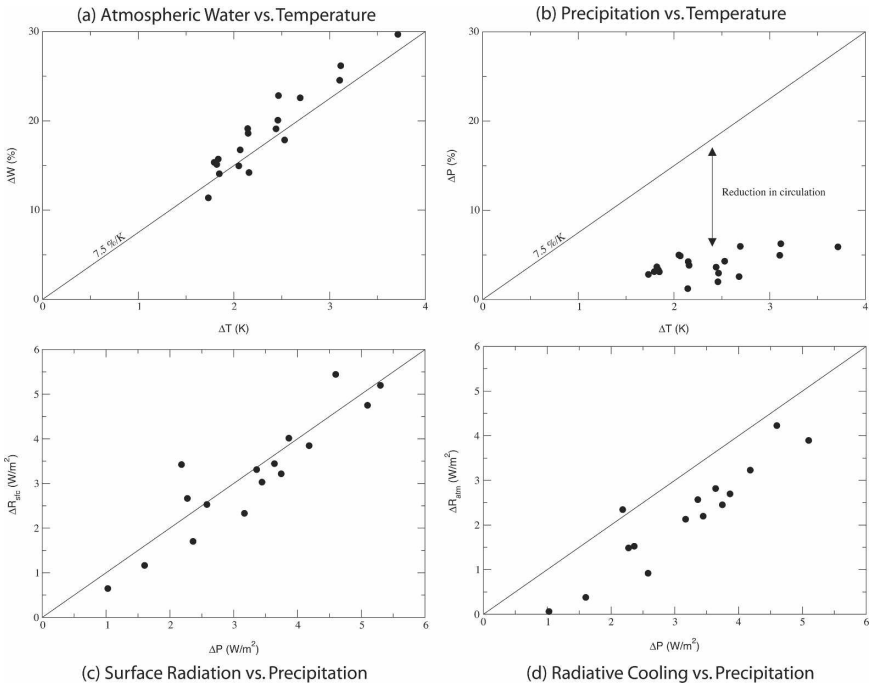

FIG. 2. Scatterplots of the change in global-mean quantities for each of the models listed in Table 1 for which the necessary data were available in the archive. Results are shown for (a) temperature vs column-integrated water vapor (%); (b) temperature vs precipitation (%); (c) precipitation (W m^{-2}) vs net downward radiation at the surface; and (d) precipitation (W m^{-2}) vs net radiative cooling of the atmosphere. The differences are computed by subtracting the decadal means from the first 10 yr and last 10 yr of the twenty-first century as projected by the A1B scenario: (2090–2100) – (2000–10). Panels (a) and (b) reproduce Figs. 2.a and 2.b of Held and Soden (2006).

umn water vapor also increases in all models. Because the mixing ratio of water vapor decreases rapidly with height, the column total is heavily weighted by boundary layer moisture. Much of the intermodel spread in the water vapor response stems from the differences in temperature response between models: models with larger warming also exhibit greater lower-tropospheric moistening.

There is a strong coupling between water vapor and temperature changes in scenario A1B of these models (Fig. 2a). While the moistening does vary from model to model, all models exhibit a nearly linear relationship between total column water vapor and surface temperature. The rate of this increase is ~7.5% K^{-1}, which is consistent with that expected from an increase in vapor pressure under the assumption of a constant relative humidity. These model results are also consistent with observational estimates in indicating that global-mean relative humidity changes are slight (e.g., Wentz and Schabel 2000; Trenberth et al. 2005; Soden et al. 2005). Although there can be significant regional changes in relative humidity (e.g., Vecchi and Soden 2007), the global-mean behavior closely resembles that expected from Clausius–Clapeyron (C–C) arguments.

b. Precipitation and convective mass flux

The fractional changes in precipitation Fig. 1c also increases in all models, with considerable variability from model to model. More importantly, the magnitude of the precipitation is roughly 1%–2% K^{-1}, much weaker than the rate of atmospheric water vapor increase (Fig. 2b).

The difference between the rate of moistening and rate of precipitation increase requires that the rate of overturning in the atmosphere weaken as the climate warms (Held and Soden 2006). Following Held and Soden (2006), we approximate the global-mean precipitation as, $P = M_c q$, where P is the precipitation, M_c is the convective mass flux, and q is a typical boundary layer mixing ratio. This assumes that precipitation is generated by air being carried from the boundary layer into the free troposphere where most of the vapor condenses and falls out as precipitation. Because the mixing ratio at the level of detrainment is at least an order

of magnitude smaller than that in the boundary layer, the return flow of vapor into the boundary layer by large-scale subsidence is negligible.

We estimate the change in M_c from P and q, assuming that q follows C–C scaling at 7% K^{-1} and taking P from the model:

$$\Delta M_c'/M_c' = \Delta P/P - 0.07\Delta T, \quad (1)$$

where the prime indicates this is an *estimate* of the mass flux, rather than the actual quantity. For the Geophysical Fluid Dynamics Laboratory (GFDL) Coupled Climate Model version 2.1 (CM2.1), the estimated mass flux agrees closely with that explicitly simulated by the model (Fig. 3a), substantiating the arguments outlined above and suggesting that one can estimate the change in convective mass flux in the other models using Eq. (1). To the extent that Eq. (1) is a valid approximation for other IPCC AR4 models, the mass flux decreases in all models, with a range of 10%–20% by the year 2100 (Fig. 3b). The relatively large range in convective weakening reflects both the differing climate sensitivities among models (Fig. 1a), as well as the range in precipitation response per unit warming of the surface (Fig. 1c). In models with weaker precipitation response the atmospheric overturning must spin down more, given the C–C rate of increasing vapor (~7% K^{-1}). The reduced convective mass flux implies a corresponding reduction in the rate of radiatively driven subsidence in the Tropics, which has also been noted in previous modeling studies (Knutson and Manabe 1995; Larson et al. 1999; Zhang and Song 2006).

c. Surface and atmospheric radiation

Given the importance of precipitation in determining the response of the atmospheric circulation, we now consider the linkages between global precipitation and the energy cycle. Global-scale changes in precipitation require compensating changes in radiative heating of the surface and troposphere, as is illustrated in Figs. 2c,d. The energy surface radiative energy balance was computed only for those models in which the necessary radiative fields were available from the AR4 archive. As noted above, ΔP in these models shows little correlation to the change in global-mean temperature or water vapor. In contrast, the global-mean precipitation response approximately balances ΔR_{sfc} (Fig. 2c) and ΔR_{atm} (Fig. 2d), with considerable variation from model to model. Models with a larger increase in R_{sfc} respond with a proportionate increase in evaporative cooling (and thus precipitation). A similar conclusion is obtained if one considers the balance between radiative cooling of the atmosphere and the release of latent heat from precipitation (Fig. 2d). Thus, attempts to understand global-mean precipitation response to a warmer climate must address its coupling to the radiative energy budget. The role of surface radiation in determining the global-mean precipitation response has been noted in many previous studies (e.g., Boer 1993; Soden 2000; Allen and Ingram 2002; Held and Soden 2006).

Modeling experiments with tropical mesoscale models also indicate that atmospheric radiative cooling increases more slowly than the atmospheric moisture in response to warming (e.g., Larson and Hartmann 2003). However, the relative importance of various feedback processes (e.g., cloud, surface albedo, water vapor, etc.) in determining the surface radiation response remains unclear. Likewise, it is not obvious why the surface radiation increases more slowly than the rate of atmospheric moistening. If the surface radiation increased at a faster rate than C–C, the arguments outlined above would imply a strengthening of the atmospheric circulation rather than a weakening.

d. Midtropospheric vertical velocity

In section 2b we argued, based on the model precipitation and water vapor changes, that convective mass flux should weaken in all the models. Unfortunately, we do not have access to the convective mass fluxes from most of the models in the PCMDI AR4 archive to test the robustness of this result directly. However, midtropospheric Lagrangian pressure tendency[3] (ω, a measure of atmospheric vertical velocity), integrated over ascending regions, weakens in all models as the climate warms (Fig. 1d). These results are qualitatively consistent with the implied changes in circulation from the precipitation and water vapor fields (see Figs. 2 and 3). Both the inferred changes in convective mass flux (section 2b) and explicitly simulated change in monthly mean upward ω_{500}^{+} indicate that the circulation weakens as the climate warms.

There is a strong correlation across models ($r = 0.86$) between the reduction in M_c' and ω_{500}^{+} (Fig. 4a). Changes are computed by differencing the means from the first 20 and the last 20 yr of the integration (2081–2100)–(2001–20). Models with a larger reduction in the M_c' also exhibit a larger reduction in ω_{500}^{+}. As M_c' is estimated from the changes in P and SST, this further supports the basic premise that the slower increase of precipitation relative to water vapor should lead to a weakening of the circulation.

[3] We here use 500-hPa pressure velocity, though the principal results are insensitive to the use of other midtropospheric levels (e.g., 400 or 600 hPa).

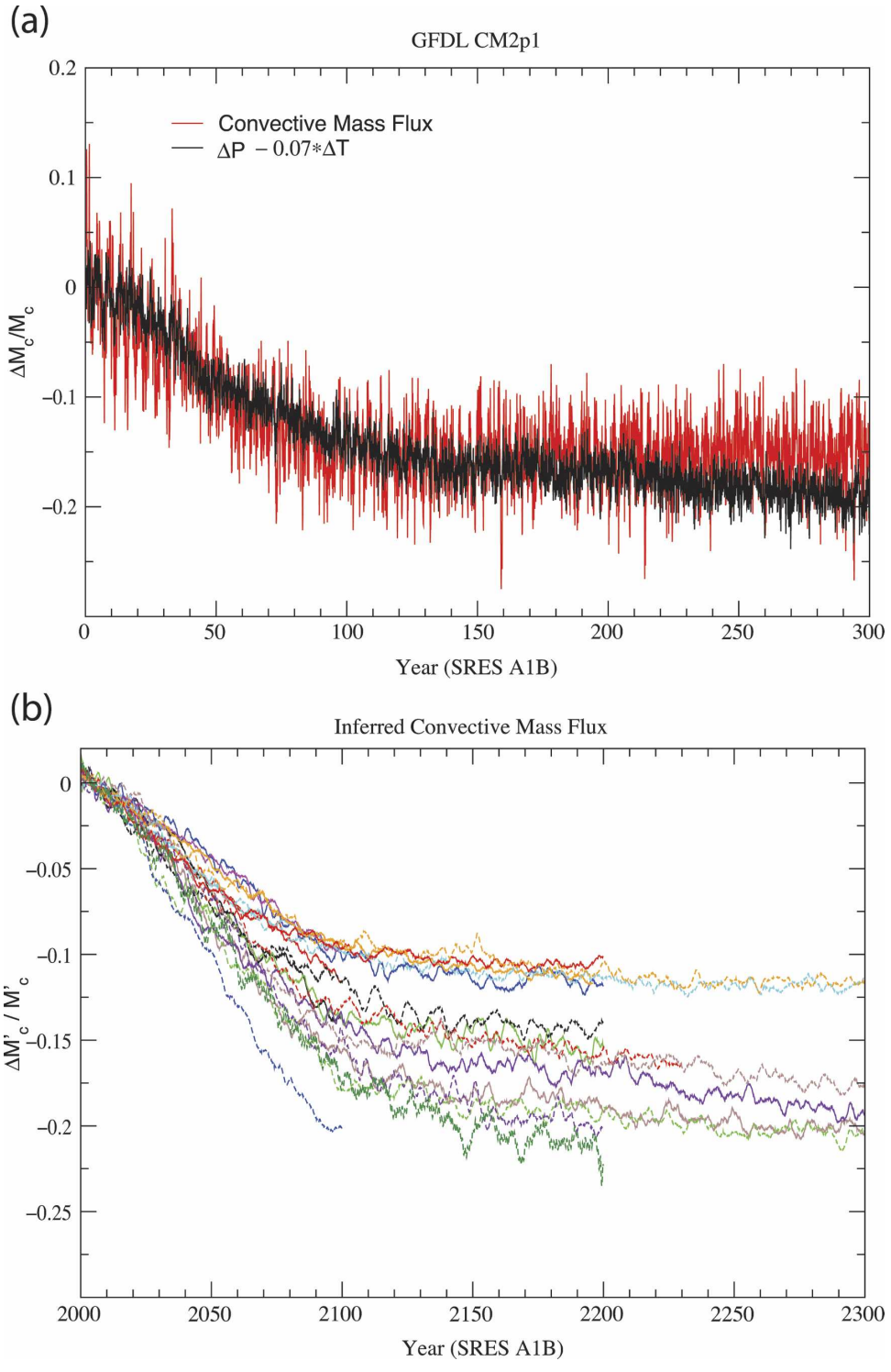

FIG. 3. (a) Monthly mean fractional changes in the global-mean subgrid-scale convective mass flux in GFDL's CM2.1 model as a function of time in its A1B scenario (red) and the corresponding change in convective mass flux predicted from Eq. (1). (b) The 5-yr smoothed change in convective mass flux for each of the IPCC AR4 models estimated using Eq. (1).

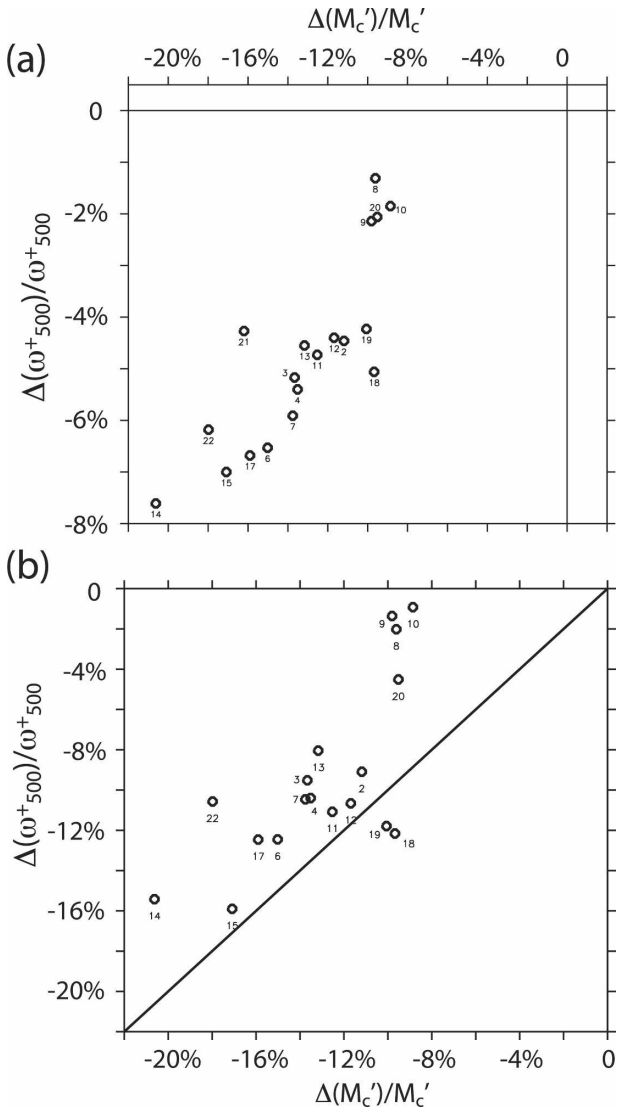

FIG. 4. (a) Scatterplot of the global-mean fractional change in upward vertical velocity at 500 hPa vs the corresponding change in estimated convective mass from Eq. (1) for each of the models listed in Table 1 for which the necessary data were available in the archive. (b) Same as in (a), except for the fractional change in upward vertical velocity with amplitude larger than 0.05 Pa s^{-1}; the 1-to-1 line is plotted. The numbers at each symbol refer to the model numbers in Table 1.

The fractional reductions of ω^{+}_{500} are much smaller than those of M'_c, the most sensitive models have up to a 20% weakening for M'_c but only a ~10% weakening for ω^{+}_{500}. We hypothesize that this may reflect the presence of nonprecipitating sources of upward motion in the midtroposphere, and that these nonprecipitating events tend to be weak and not associated with moisture transport from the boundary layer (e.g., gravity waves). If we neglect weak values of upward motion (e.g., values of monthly mean $\omega^{+}_{500} < -0.05$ Pa s^{-1}), then the magnitude of the ω^{+}_{500} reduction is consistent with that inferred from M'_c, for all but a handful of models. Figure 4b shows an equivalent plot to Fig. 4a, except for ω^{+}_{500} with upward amplitude in excess of 0.05 Pa s^{-1}; for all but the three Goddard Institute for Space Studies (GISS)[4] models, the magnitude of the ω^{+}_{500} reduction in Fig. 4b is increased relative to that in Fig. 4a, and is comparable to that of M'_c. This also indicates that the changes in upward vertical velocity are more pronounced for the stronger values of ascent than for the weaker ones. Since the threshold of -0.05 Pa s^{-1} is somewhat arbitrary, for the rest of the manuscript, we use as our circulation metric the change in upward ω^{+}_{500} shown in Fig. 4a because it is explicitly simulated by the model and well correlated with M'_c.

We now examine the change in the frequency of occurrence of ω^{+}_{500} as a function of the updraft strength using daily output from the GFDL CM2.1 over the entire globe (Fig. 5). In this model the reduction in the mean ω^{+}_{500} is manifest in the daily data as a reduction in frequency of the strongest upward motions (e.g., percentile bins >50%) and an increase in frequency of the weakest upward motions (e.g., percentile bins <50%), with the largest changes occurring at the extremes of the distribution. There is also a reduction in the total number of grid points with upward ω^{+}_{500}: in GFDL CM2.1, the circulation weakens by producing fewer and less intense updrafts. The reduction in updraft frequency is qualitatively consistent with the "upped-ante mechanism" (Chou and Neelin 2004). To the extent to which daily, gridpoint ω^{+}_{500} provides a proxy for the dynamical intensity of weather systems, the frequency of the most intense events is projected to decrease in this particular model. The lack of daily vertical velocity fields in the AR4 archive prevents us from investigating the robustness of this behavior across other models. The models used here are too coarse to resolve convective updrafts explicitly; thus, they may not be able to represent all changes in the characteristics of convection.

It is important to note, however, that this should not be interpreted as a reduction in the frequency of intense precipitation events; intense precipitation events become more frequent in GFDL CM2.1 as the climate warms. A similar analysis of the statistical distribution of daily precipitation rates (Fig. 5b) indicates that the frequency of the most intense rain events (e.g., 95%–100% range) increases; in this model, the boundary

[4] For the three GISS models, outside of regions with strong orographic variations there are few grid points with upward ω^{+}_{500} larger than 0.05 Pa s^{-1}; this may be because of the relatively low resolution of the atmospheric components of these models.

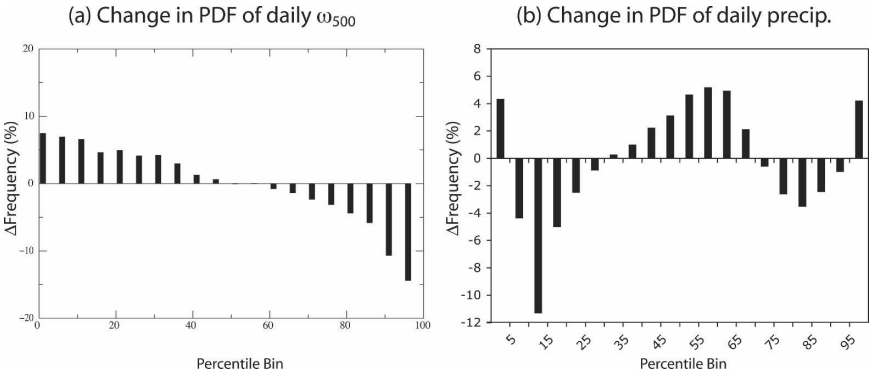

FIG. 5. The percentage change in the frequency of occurrence of (a) ω_{500}^{+} as a function of updraft strength, and (b) precipitation as a function of precipitation intensity, using daily output from the GFDL CM2p1 for the entire globe. The distribution function was calculated using 20 bins, each of which contains 5% of the total distribution for the control (e.g., 0%–5%, 5%–10%, etc.). The thresholds for each bin were computed using the first 5 yr of the A1B integration (2000–05). The same bin thresholds were then used to compute the distribution over the last 5 yr of the twenty-first century (2095–2100) from the same integration. The plot depicts the percentage change in each bin between the last 5 yr and first 5 yr of the twenty-first century under the A1B scenario.

layer water vapor increases enough to compensate for the reduced intensity of updrafts and result in a net increase in heavy rain events. Conversely, one need not interpret an increase in extreme precipitation events as an indication of increase in extremes in circulation (as illustrated here by the GFDL CM2.1).

e. Spatial structure of circulation changes

Following Held and Soden (2006) we consider the spatial variance over the Tropics of the upward pressure velocity as another measure of the strength of the circulation, and we divide this variance into its zonal-mean and zonally asymmetric (or stationary eddy) components. To the extent that the weakening of the upward vertical velocity is proportional to the preexisting velocity field, its spatial variance should also decrease at roughly twice the rate of the mean. To verify this, changes in the total, zonal-mean, and stationary eddy variance are computed over the Tropics (30°N–30°S) for ω_{500}^{+} by differencing the first and last 10 yr of the twenty-first century. Figure 6 plots the change in total variance versus the change in zonal-mean and stationary eddy variance for each model.

In all models except one, the total spatial variance in upward vertical velocity over the Tropics decreases as the climate warms. In all models the reduction in total variance is dominated by a reduction in the zonally asymmetric component (Fig. 6): the zonally asymmetric part of the tropical circulation (e.g., the Walker cell) weakens more than the zonally symmetric part (e.g., the Hadley cell). The tendency of the zonally asymmetric component of the circulation to weaken more than the zonally symmetric component was noted by Held and Soden (2006) and Lu et al. (2007).

A weakening in the Walker circulation is also evident in a map of the multimodel ensemble-mean change in midtropospheric vertical velocity (ω_{500}; Fig. 7b). For each model the change is computed by differencing the decadal-mean ω_{500} from the first and last 10 yr of the

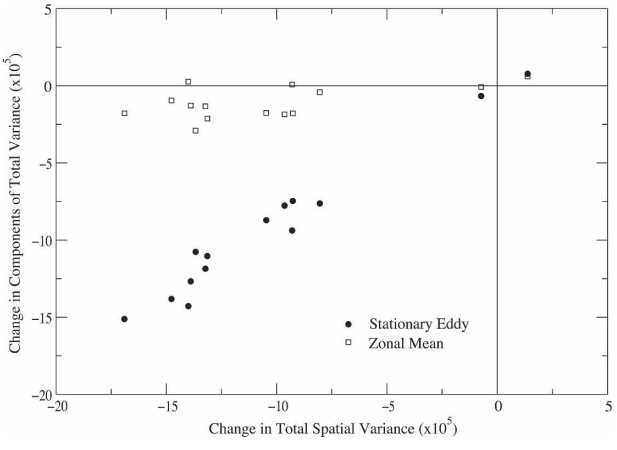

FIG. 6. Scatterplot of the change in spatial variance of ω_{500}^{+} over the Tropics. Results are shown separately for the change in zonal-mean (open) and stationary eddy (filled) components of the variance as a function of the change in total variance. The differences are computed by subtracting the decadal means from the first 10 yr and last 10 yr of the twenty-first century as projected by the A1B scenario: (2090–2100) − (2000–10).

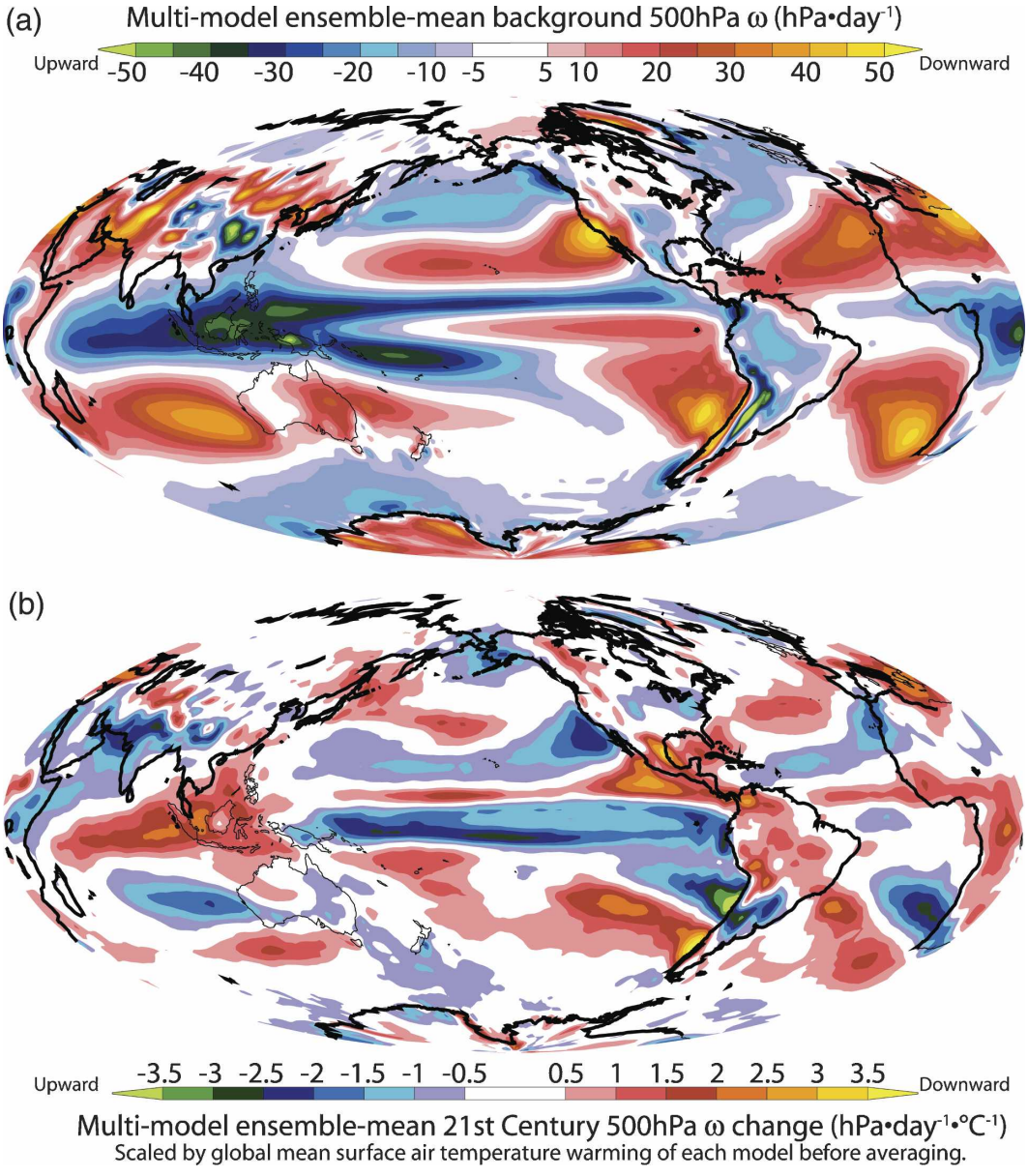

FIG. 7. The multimodel (a) ensemble-mean ω_{500} and (b) ensemble-mean change in ω_{500} per degree global warming; positive values are downward. The change is computed by differencing the decadal-mean ω_{500} from the first and last 10 yr of the twenty-first century, normalizing this difference by the change in global-mean temperature for each model, and then averaging the result across all models. Units: (top) hPa day^{-1} and (bottom) hPa day^{-1} K^{-1}.

twenty-first century, normalizing this difference by the model's change in global-mean temperature; the results represent the change in vertical velocity per degree global warming. For reference, the ensemble-mean climatology of ω_{500} for the first 10 yr of the twenty-first century is also depicted in Fig. 7a.

The ω_{500} changes are almost everywhere in opposite sense to the background ω_{500}, with the notable exception of the central equatorial Pacific where the eastward shift in convection acts to reinforce the preexisting ascending motions already found there. A poleward shift of the subtropical subsidence regions is also evident (e.g., Lu et al. 2007). The most pronounced changes in ω_{500} occur primarily over the tropical Pacific where the ascending air over Indonesia weakens by ~2 hPa day^{-1} K^{-1} global warming. Likewise, the descending air over the subtropical high pressure regions in the eastern Pacific weakens at a similar rate. These changes

imply a weakening in the zonal overturning of air across the equatorial Pacific at a rate of roughly 5%–10% K^{-1} of global warming.

The weakening of circulation and eastward shift of convection is also evident in the ensemble-mean precipitation response of the models (Fig. 8); the ensemble-mean changes for both fields were computed for the same periods as in Fig. 7, and normalized by the global-mean surface temperature response of each model before averaging. Note that the region of largest fractional increase in precipitation and with relatively large warming in the tropical oceans in the central equatorial Pacific coincides with the region of enhanced upward motion (Fig. 7). Figure 8c displays the difference between the rate of C–C moistening (7% K^{-1}) based on the ensemble-mean surface air temperature change (Fig. 8a) and the ensemble-mean rate of precipitation change (Fig. 8b). The local rate of precipitation increase is smaller than the rate of atmospheric moistening, except for in the central and eastern equatorial Pacific and the western Indian Oceans, indicating that changes in the atmospheric circulation are acting to reduce the precipitation over most of the model domain. This pattern of "dynamic" precipitation response is also consistent with that obtained by Emori and Brown (2005) based on a compositing analysis of precipitation anomalies using midtropospheric vertical velocity.

f. Sea level pressure and the Walker circulation

As argued above, the large-scale weakening of the atmospheric overturning circulation in the Tropics occurs principally through the zonally asymmetric component of large-scale circulation, a dominant component of which is the Pacific Walker circulation. In this subsection, we show that the weakened Walker circulation is also reflected in the model-simulated changes in sea level pressure (SLP).

There are various measures one can use to assess the strength of the Walker circulation, including 200-hPa velocity potential (e.g., Tanaka et al. 2004) and SLP (e.g., Walker and Bliss 1932, 1937; Vecchi et al. 2006; Zhang and Song 2006). Among the advantages of SLP as a measure of the Walker circulation are that it is a regularly measured both on land at and sea, and that records of it exist into the midnineteenth century. Our measure of the Walker circulation is the SLP difference between the eastern Pacific (5°S–5°N, 160°–80°W) and the Indo-West Pacific (5°S–5°N, 80°–160°E), which we label *d*SLP. Variations in *d*SLP are strongly correlated in time and across models with the strength of equatorial Pacific zonal-mean zonal wind stress in both observations and models (e.g., Clarke and Lebedev 1996; Vecchi et al. 2006).

Figure 9a shows a scatterplot of normalized *d*SLP change versus normalized ω^{+}_{500} change for scenario A1B of 16 of the IPCC AR4 models listed in Table 1.[5] We use differences between the first 20 and last 20 yr of the twenty-first century as a measure of change in a quantity. The models tend to show a weakening of the Walker circulation in response to CO_2 increase: all but two of the models in Fig. 9 show a weakening of *d*SLP over the first 100 yr of scenario A1B. The two models in Fig. 9 that show a strengthening are the Institute of Numerical Mathematics (INM; a 6% increase) and GISS Atmosphere–Ocean Model (AOM; a 22% increase)—GISS-AOM has a deficient Walker circulation, with a reference *d*SLP that is less than a third of that observed.

In Fig. 9a it is evident that there is a relationship between the relative changes in ω^{+}_{500} and *d*SLP across the different models: the models with larger ω^{+}_{500} weakening tend to have a larger weakening in *d*SLP. The correlation coefficient between $\Delta\omega^{+}_{500}/\omega^{+}_{500}$ and $\Delta d\text{SLP}/d\text{SLP}$ is 0.73; intermodel differences in the ω^{+}_{500} change explain ~50% of intermodel differences in the *d*SLP change.

The weakening of the large-scale zonal gradient of SLP (*d*SLP) is a dominant feature of SLP change in the multimodel ensemble-mean response to global warming. Figure 10a shows a map of the ensemble-mean change in SLP (ΔSLP) computed following the same method as in Fig. 8 for ω^{+}_{500}. There is a clear pattern of decreasing SLP over the eastern tropical Pacific and increasing SLP over the western Pacific–Indonesian region, consistent with a weakening of the Walker circulation. The spatial structure of the tropical Pacific SLP changes in Fig. 10a correspond closely with those in the observational record (Vecchi et al. 2006; Zhang and Song 2006). In addition to a weakening of the Pacific Walker circulation, the ensemble mean also exhibits a weakening of the equatorial Indian Ocean zonal SLP gradient.

Overall, these models show a tendency toward a

[5] Three models are omitted from Fig. 9a because they have extremely deficient Walker circulations, one (GISS E-R) has a reference *d*SLP of only 1.6 Pa (observed *d*SLP is ~180 Pa), and two (CGCM3.1 T47 and CGCM3.1 T63) have a reference *d*SLP that is of the opposite sign as that observed. Three other models (BCCR-CM2.0, CSIRO Mk3.0, and MIUB ECHO-G) were omitted from Figs. 9a and 11 because the atmospheric vertical velocities were not available from the IPCC-AR4 archive. BCCR-CM2.0 and CSIRO Mk3.0 show a decrease in *d*SLP, while MIUB ECHO-G shows an increase.

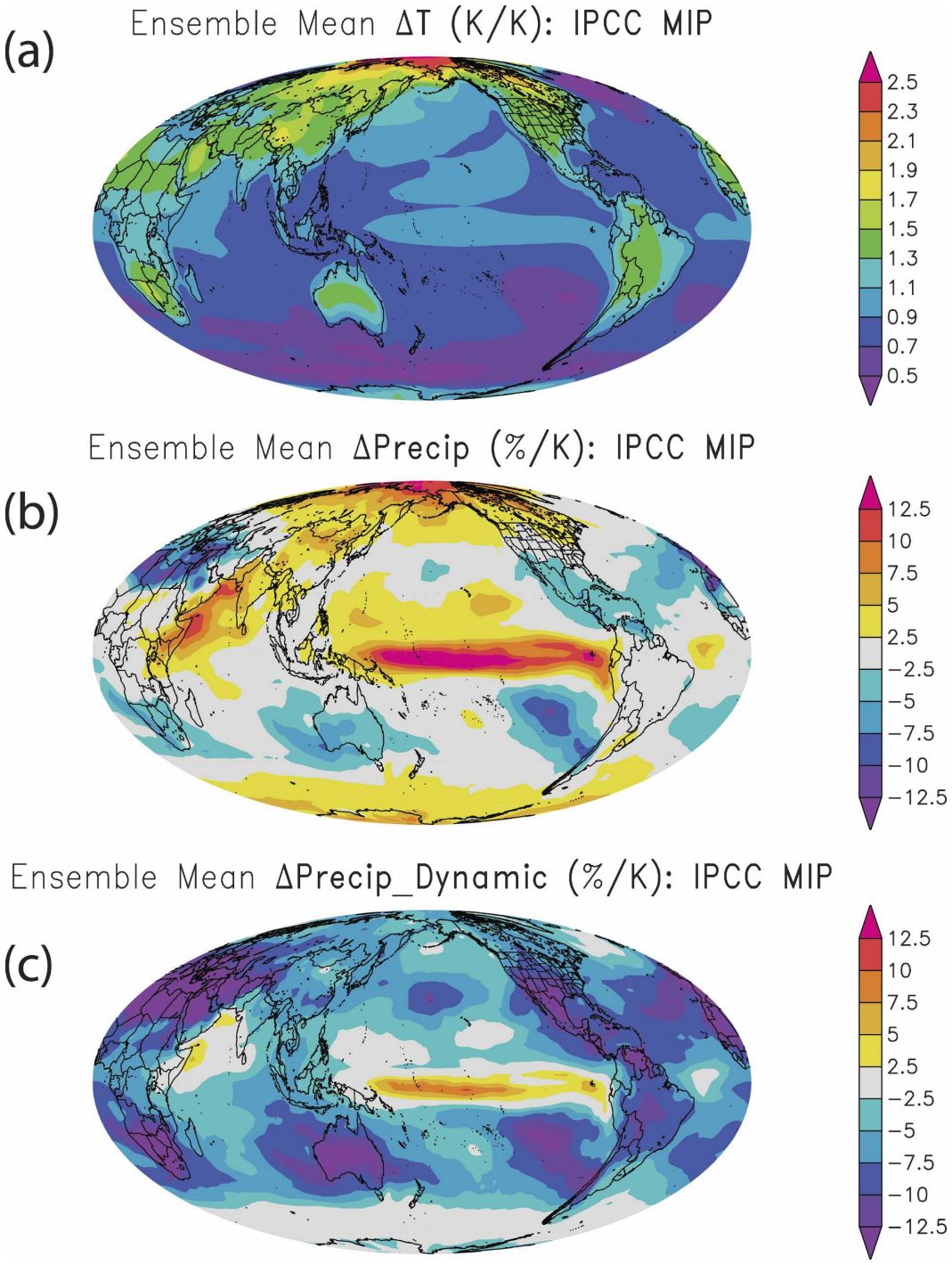

FIG. 8. The multimodel ensemble-mean (a) changes in surface air temperature and (b) percentage change in precipitation per degree global warming. (c) The difference between the rate of C–C moistening (7% K^{-1}) based on the ensemble-mean surface air temperature change [(a)] and the ensemble-mean rate of precipitation increase [(b)]. The ensemble-mean changes for all fields were computed for the same periods as in Fig. 7, and the results for each model are first normalized by the global-mean temperature response before averaging across the ensemble of models. Units: (a) K K^{-1} and (b),(c) % K^{-1}.

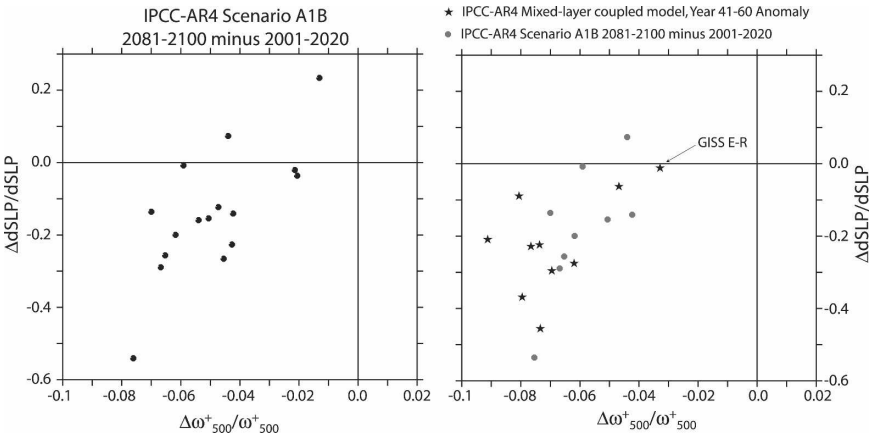

FIG. 9. (left) Scenario A1B scatterplot of the fractional change in the zonal SLP gradient (dSLP) vs fractional change in upward vertical velocity (ω^{+}_{500}) for the period 2100–2090 minus 2010–2000. (right) Scatterplot of slab model response to CO_2 doubling, the fractional change in the zonal SLP gradient (dSLP) vs fractional change in upward vertical velocity (ω^{+}_{500}). Stars show the response of 10 mixed layer coupled models' doubled CO_2, anomalies computed from control run over years 41–60. Gray circles show the scenario A1B fraction change in dSLP and ω^{+}_{500} for the same nine models (GISS-ER is not shown for scenario A1B).

more "El Niño–like" state in the Walker circulation, which is more robust than that found by van Oldenborgh et al. (2005, hereafter vOPC05) for the same models. vOPC05 used the first empirical orthogonal function (EOF) of tropical Indo-Pacific SLP as a measure of the "El Niño-ness" of the system. This apparent discrepancy between vOPC05 and this paper can be understood by comparing the spatial structure of the EOFs in their Fig. 9 with our Fig. 10. The ensemble-mean change in SLP from these models (Fig. 10a) has a narrower meridional structure than the principal pattern of Indo-Pacific SLP variability in these models

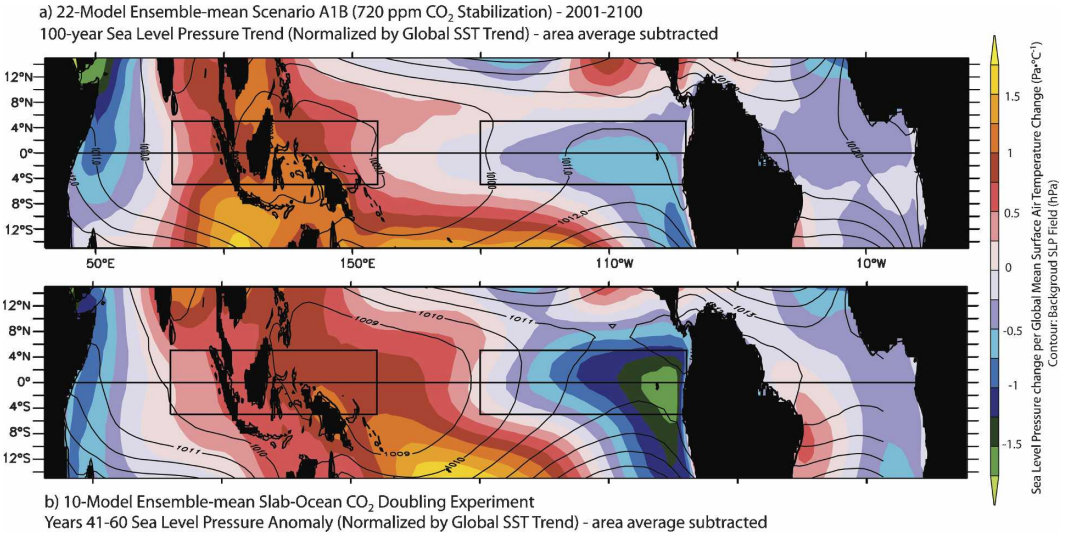

FIG. 10. Multimodel ensemble-mean sea level pressure changes forced by increased CO_2 (shading) and reference SLP field (contours). (a) The 22-model average of the linear least squares trend of SLP over 2001–2100 of scenario A1B, with each model normalized by the global-mean surface temperature trend over the same period; the reference is the average over 2001–20 (hPa). (b) The 10-model average of the year 41–60 SLP anomaly from the ocean mixed layer coupled experiments forced by 2 × CO_2 (anomalies computed by subtracting mixed layer control run over same period); the reference is the year 41–60 average from the control run (hPa). Black boxes indicate regions used to compute SLP-based Walker circulation index (dSLP).

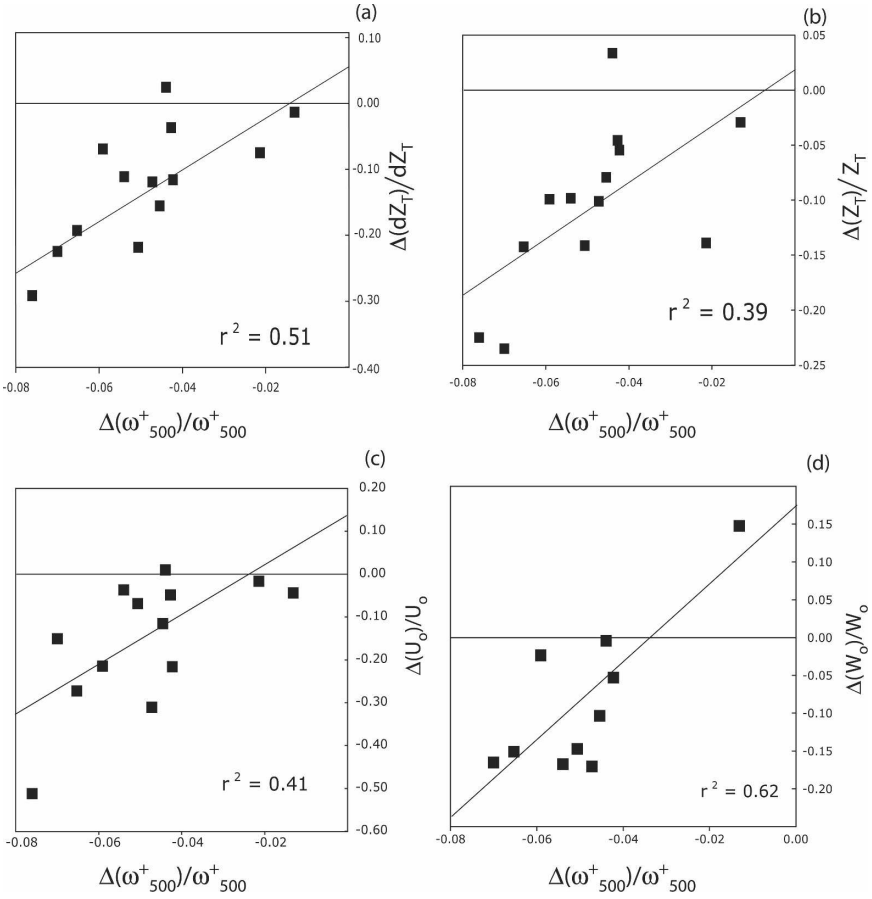

FIG. 11. Scatterplots of fractional change in midtropospheric upward motion and equatorial Pacific Ocean fractional changes. In all panels the horizontal axis is $\Delta\omega^{+}_{500}/\omega^{+}_{500}$. Vertical axes are (a) the change in thermocline zonal slope across equatorial Pacific divided by initial slope; (b) the change in zonal-mean thermocline depth across equatorial Pacific divided by initial depth; (c) the change in equatorial Pacific zonal-mean surface current divided by initial surface current; and (d) the change in equatorial Pacific vertical velocity (averaged 0–200 m, 2°S–2°N, 180°E–80°W) normalized by initial vertical velocity. The intermodel difference in change of midtropospheric upward motion explains close to 50% of the intermodel variance in the oceanic quantities considered.

(shown in Fig. 9 of vOPC05). So, even though the SLP changes resemble El Niño in that they show a relaxation of the zonal SLP gradient across the Indo-Pacific (our Figs. 9 and 10), the structure of the SLP changes is distinct from the principal pattern of interannual SLP variability.

The Walker circulation response to global warming deviates from that associated with El Niño in another, more fundamental, manner: it does not feed off dynamical changes in the ocean. The weakening of the Walker circulation in response to increased CO_2 is also present in climate models, which use a mixed layer slab ocean model; that is, in models with fixed implicit ocean dynamics. The last column in Table 1 indicates the models for which mixed layer output was available. Figures 9b[6] and 10b show the corresponding relationships between ω^{+}_{500} and dSLP and the ensemble-mean ΔSLP, respectively, for the available slab ocean models. For the slab models, the differences are computed using the equilibrated response from a set of $2 \times CO_2$ climate change simulations (averaged over 20 model years).

Dynamical ocean changes are not necessary for the weakening of the Walker circulation in response to a warming climate. In fact, Fig. 10b shows that the re-

[6] The slab version of GISS-ER is plotted in Fig. 9b, even though no equivalent scenario A1B point is plotted (because of the deficient reference Walker circulation). The GISS-ER point is highlighted with an arrow.

sponse of the SLP gradient across the equatorial Pacific (per unit global warming) is stronger in models without dynamical ocean adjustments (this relationship still holds when Fig. 10a is repeated with only the 10 scenario A1Bs for which slab runs are available). In a warming world, the coupled response to dynamical ocean changes acts to counter the weakening of the Walker circulation induced by atmospheric thermodynamic constraints.

Further comparisons between the response of the ocean mixed layer slab coupled model to doubling CO_2 and those of the fully coupled scenario A1B models highlight the dominant role of the atmospheric processes to the response of the Walker circulation. The ω_{500}^{+} and dSLP response of the slab and fully coupled versions of the nine models shown in Fig. 9b are strongly correlated: the intermodel correlation of the slab and scenario A1B $\Delta\omega_{500}^{+}/\omega_{500}^{+}$ is 0.72, and the intermodel correlation of the slab and scenario A1B ΔdSLP/dSLP is 0.82. Thus, the atmospheric model parameterizations have a dominant control on the response to global warming of both the overall atmospheric overturning circulation and the Walker circulation.

3. Oceanic response

Variations in the intensity of the Walker circulation (as diagnosed from SLP) are tied to changes in the strength of the surface winds in the equatorial Pacific Ocean (e.g., Clarke and Lebedev 1996; Vecchi et al. 2006). Theoretical considerations, numerical experiments, and observations of the response of the equatorial oceans to changes in surface wind suggest certain responses of the equatorial Pacific Ocean to a sustained weakening of the Pacific equatorial easterlies induced by a slowing Walker circulation, among them: (i) a weakening of the surface westward currents, (ii) a weakening of equatorial upwelling, (iii) a relaxation of the east–west thermocline gradient, and (iv) a reduction of the mean depth of the equatorial thermocline (e.g., Cane and Sarachik 1977; Cane 1979; Philander 1981; McPhaden 1993; Clarke and Lebedev 1997; Jin 1997; Kirtman 1997; McPhaden 1999; Wittenberg 2002). These are not the only quantities one would expect to be impacted by a slowing Walker circulation, but they offer an illustration of the implications of slowing atmospheric overturning to tropical oceanic circulation.

Figure 11 shows scatterplots of the fractional change in ω_{500}^{+} for each model against the corresponding fractional change in the following: the thermocline zonal slope across the equatorial Pacific (dZ_T), zonal-mean thermocline depth across the equatorial Pacific (Z_T), the equatorial Pacific zonal-mean surface current (U_o), and the equatorial Pacific zonal-mean upper-ocean vertical velocity (W_o). For each quantity the correlations exceed 0.68, indicating that ~50% of the intermodel variance in the oceanic response can be explained (statistically) in terms of the weakened atmospheric circulation. The atmospheric circulation changes are, in turn, related to the rate of precipitation increase relative to C–C. Thus, to a substantial extent, the response of the equatorial Pacific oceanic circulation to an increase in atmospheric CO_2 is constrained by the response of global precipitation and temperature. In the following subsections we explore the changes in each of these oceanic quantities in greater detail by examining their multimodel ensemble-mean response, and highlight those features that are consistent with a slowing Walker circulation.

a. Tropical ocean thermal structure

The dominant feature of the 2001–2100 Z_T changes (ΔZ_T) for the IPCC AR4 models multimodel ensemble mean is a shoaling of the western equatorial Pacific Z_T (Fig. 12a), associated with a reduction of both the zonal-mean Z_T and the zonal slope of Z_T (dZ_T; see Fig. 13). For our analysis we define the Z_T as the vertical location of the maximum vertical gradient of monthly mean temperature.[7] Even though zonal-mean equatorial Pacific Z_T can be influenced by nonlocal factors and vary independently from dZ_T (e.g., Boccaletti et al. 2004; Fedorov et al. 2006), for the IPCC AR4 models they principally result from a common cause: the intermodel correlation coefficient of ΔdZ_T and ΔZ_T is 0.82. This Z_T behavior is consistent with the oceanic response to a long-term, meridionally narrow, weakening of the equatorial easterlies, which should result in both a reduction of the dZ_T and a reduction in Z_T (e.g., Philander 1981; Jin 1997; Clarke and Lebedev 1997;

[7] We must define "thermocline depth" (Z_T) in order to explore its changes. A common technique is to use the depth of a particular isotherm as a proxy for Z_T (e.g., Harrison and Vecchi 2001; Zelle et al. 2004); in the tropical Pacific the 20°C isotherm is often used. However, this type of metric is problematic in multimodel climate change analyses because 1) the isotherm that is representative of the thermocline varies from model to model, 2) in a changing climate the isotherms that are representative of the thermocline will change over time, and 3) the change in the isotherm representative of the thermocline is model dependent (a function of, among other aspects, climate sensitivity of the model, diapycnal mixing, etc). An alternative method is to define Z_T as the vertical location of the maximum in the vertical gradient of temperature. Though at a time–space point the only possible values from this definition are the discrete depths of the vertical coordinate system of each model, when the values are averaged over regions in space and time more subtle changes can be deduced.

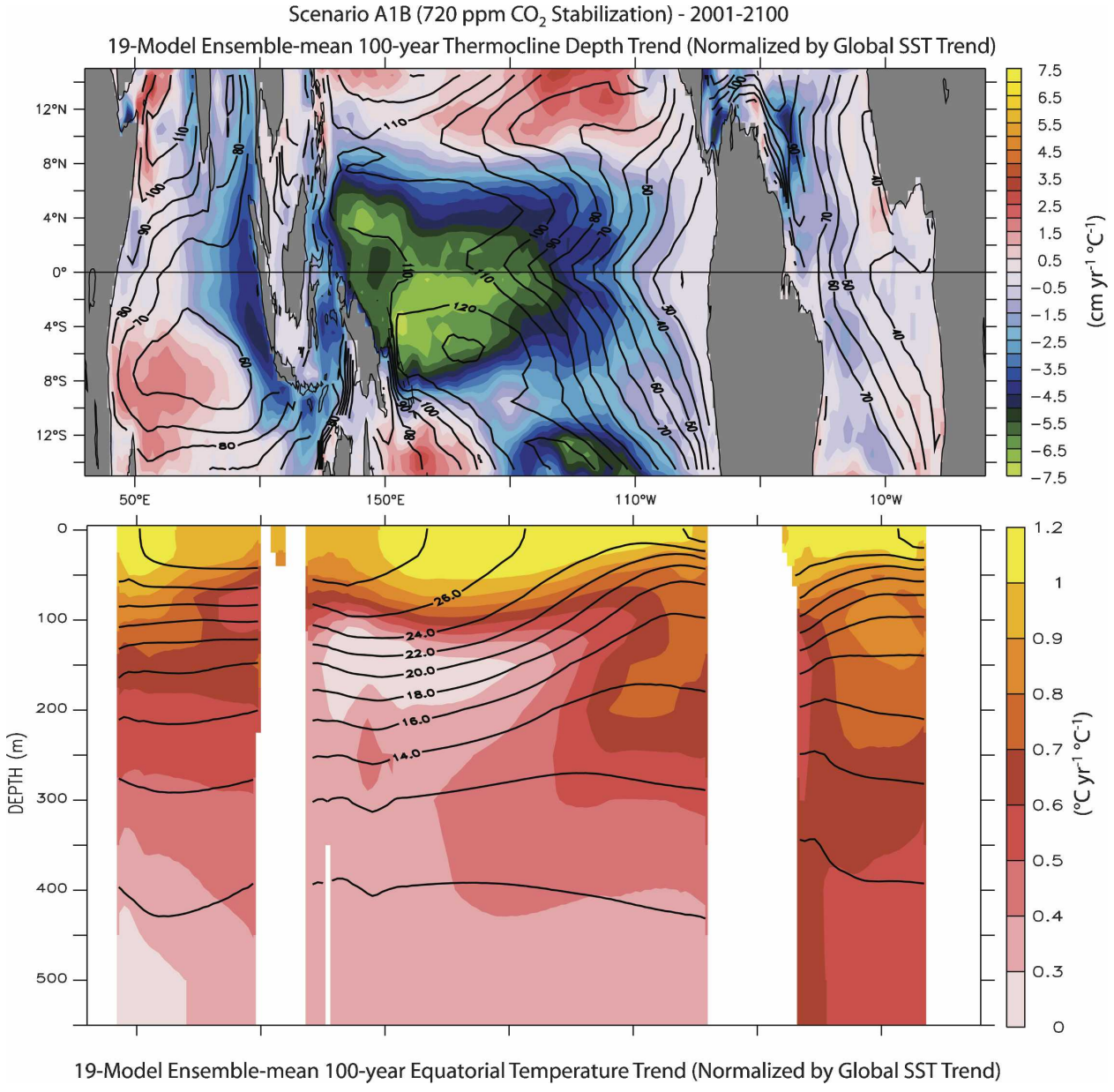

FIG. 12. Multimodel ensemble-mean tropical ocean thermal structure trends forced by increased CO_2 (shading) and reference (contours). (top) The thermocline depth changes. (bottom) The 2°S–2°N averaged temperature changes over the upper 500 m. Trends are the 19-model average of the linear least squares trend of each quantity over 2001–2100 of scenario A1B (see Table 1), with each model normalized by the global-mean surface temperature trend over the same period. The reference is the 2001–20 average of thermocline depth (top, m) and 2°S–2°N temperature (bottom, °C).

Kirtman 1997; An and Wang 2000; Wittenberg 2002), which both flattens the Z_T (in response to the equatorial westerlies) and shoals the equatorial Z_T (from anomalous ocean divergence driven by off-equatorial wind stress curl). The observed evolution of the equatorial Pacific Z_T and zonal winds over the last 50 yr is consistent with their relationship in these model projections for a warming world: as the equatorial Pacific easterly winds have weakened, the west Pacific thermocline has shoaled and the east Pacific thermocline has remained relatively unchanged (Clarke and Lebedev 1997; Vecchi et al. 2006). However, the extent to which the Pacific thermocline changes over the past 50 yr are the result of changes in global radiative forcing is not clear (e.g., Vecchi et al. 2006).

The relative intensity of both the mean equatorial

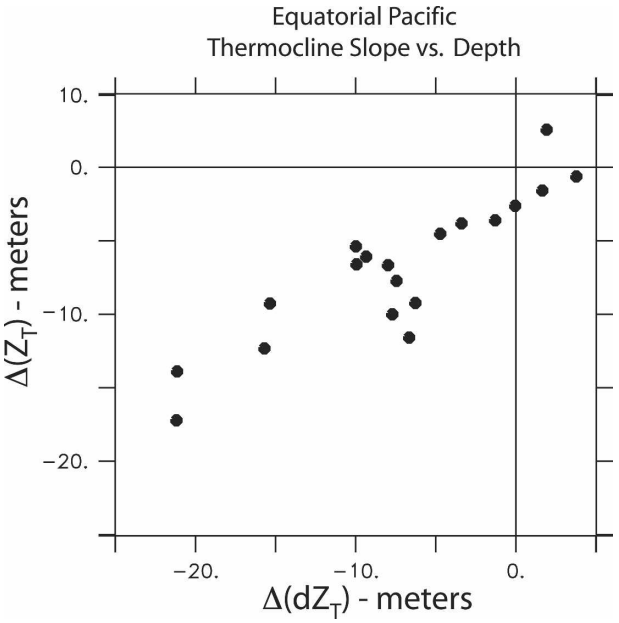

FIG. 13. Change in equatorial Pacific thermocline depth vs change of equatorial Pacific thermocline slope for scenario A1B of 19 IPCC AR4 models with available data (see Table 1). Horizontal axis shows the change in equatorial Pacific thermocline slope (difference between thermocline depth averaged 3°S–3°N, 130°–170°E and that averaged 3°S–3°N, 120°–80°W). Vertical axis shows the mean equatorial Pacific thermocline depth (averaged 130°E–80°W, 3°S–3°N). Change for each quantity is the difference between the 2081–2100 average and the 2001–20 average.

Pacific Z_T shoaling and the weakening of the equatorial Pacific dZ_T are related to the relative slowdown of the atmospheric overturning circulation across the various IPCC AR4 models (Figs. 11a,b). The intermodel variations in the fractional change in ω_{500}^{+} explain about 50% of the intermodel fractional change in equatorial Pacific dZ_T and Z_T; thus, the correlation coefficients are 0.72 and 0.67, respectively.

The multimodel ensemble also indicates Z_T changes in the tropical Indian Ocean that are suggestive of a weakening zonal atmospheric overturning circulation: a shoaling of the eastern equatorial Indian Ocean Z_T and a deepening of the off-equatorial Indian Ocean Z_T (Fig. 12a). Alory et al. (2007) suggest that anomalous Indonesian Throughflow (ITF) transport, in response to weakened equatorial Pacific easterlies, may play a primary role in the eastern Indian Ocean thermocline shoaling.

The effect of the equatorial Z_T changes can be seen in the subsurface temperature trends of the multimodel ensemble (Fig. 12b). The equatorial warming of the ocean is surface intensified, with the Indian and Pacific basins showing a stronger surface intensification than the Atlantic: the vertical temperature gradient across the equatorial thermocline is increased in these models. Though weaker than the surface warming, the east Pacific, Atlantic, and western Indian Ocean thermoclines warm fairly robustly, by 0.7°–1.0°C °C^{-1} of global surface warming. Meanwhile, the western Pacific and eastern Indian Oceans exhibit a local minimum in the warming at the thermocline, reflecting the thermocline shoaling. The multimodel ensemble western equatorial Pacific thermocline warms by <0.3°C °C^{-1} surface warming. In some models, the western equatorial Pacific Z_T shoaling results in net local cooling at thermocline depth; the counterintuitive outcome in these models is that global warming results in subsurface western equatorial Pacific cooling.

b. *Tropical ocean circulation*

The multimodel ensemble-mean linear trend in the zonal surface current (U_o) in the tropical Indian and Pacific Oceans (Fig. 14) is characterized by the reduction in the intensity of the principal zonal surface current features. In the Pacific the westward South Equatorial Current (SEC) weakens, as does the eastward North Equatorial Countercurrent (NECC); while in the Indian Ocean there is a tendency for more westward flow at the surface.

The principal features of the multimodel ensemble-mean linear trend in near-equatorial oceanic vertical velocity (W_o) include an increase in upwelling in the eastern Indian Ocean and a weakening of the equatorial Pacific upwelling (Fig. 15). These ensemble-mean changes are consistent with weakening zonal surface wind convergence over the Maritime Continent, resulting from a weakened Walker circulation. In the Indian Ocean, the anomalous equatorial easterlies result in enhanced Ekman divergence and anomalous equatorial upwelling. The near-surface reduced upwelling in the western equatorial Pacific (centered around 150°E) results from Ekman convergence forced by the westerly wind anomalies, while the reduction in deep upward motion in the eastern equatorial Pacific appears largely related to a flattening in the east–west slope of the Equatorial Undercurrent (EUC). The weakening of the SEC and the reduction in equatorial upwelling was also seen in the twentieth-century integrations using GFDL CM2.1, a model that also showed a substantial weakening of the Walker circulation (Vecchi et al. 2006).

The magnitudes of the changes in equatorial Pacific zonal and vertical currents in the various IPCC AR4 models scale well with the changes in atmospheric overturning circulation (Figs. 11c,d). About half of the intermodel variance in $\Delta U_o/U_o$ and close to two-thirds of that in $\Delta W_o/W_o$ are explained by a linear regression to

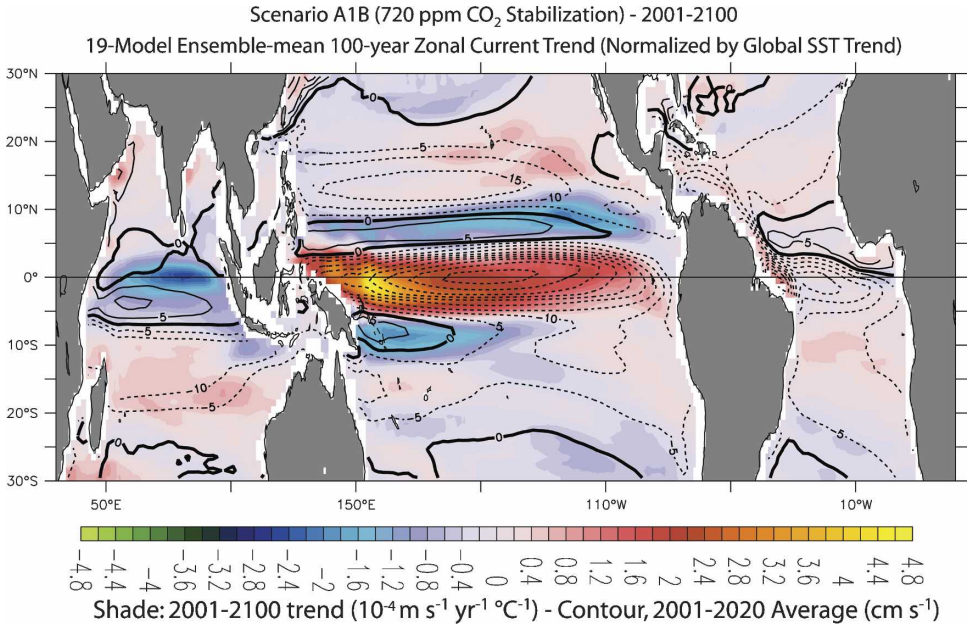

FIG. 14. Multimodel ensemble-mean tropical ocean surface zonal current trends forced by increased CO_2 (shading) and reference (contours). Surface current defined as that of the upper grid box of each model. Shading shows the 19-model average of the linear least squares trend of surface zonal current over 2001–2100 of scenario A1B, with each model normalized by the global-mean surface temperature trend over the same period. Reference is the 2001–20 average. Units: cm s^{-1}.

$\Delta\omega^{+}_{500}/\omega^{+}_{500}$. A similar relationship exists for changes in vertical velocity of the equatorial Pacific east of the date line (not shown), where 54% of the intermodel variance is explained.

The reduction of the shallow Pacific overturning in the ensemble-mean model can also be seen in Fig. 16, which shows the multimodel ensemble trend in Pacific-mean meridional velocity (averaged 130°E–80°W), scaled by the global-mean temperature change; contours indicate the reference Pacific-mean meridional velocity. The tendency of the ensemble mean is to reduce the near-equatorial shallow overturning (Figs. 15–16) equatorward of 6° the changes oppose the reference velocities. The reduction in atmospheric circulation modifies the near-equatorial shallow meridional overturning circulation in the near-equatorial Pacific, and the exchange of water between the thermocline and the mixed layer.

Recent observations indicate that, between the 1950s and the 1990s, there was a decrease in the shallow overturning circulation in the tropical Pacific (McPhaden and Zhang 2002), with a rebound between 1998 and 2004 (McPhaden and Zhang 2004). The timing of the observed decrease in circulation is consistent with the observed decadal variations in the strength of the Walker circulation, which showed a strong decrease in intensity through between the 1950s and 1998, and a modest intensification since 1998 (Vecchi et al. 2006; Zhang and Song 2006). Most models in the IPCC AR4 database were unable to reproduce the observed decrease in the late twentieth century; the Model for Interdisciplinary Research on Climate, high-resolution version [MIROC(hires)] was the only model showing a substantial weakening (Zhang and 2006). Additional studies are needed to better understand the relationship between the observed weakening in the Walker circulation and the tropical Pacific Ocean shallow meridional overturning, and the extent to which the weakening in ocean circulation represented a response to global warming or internal climate variability.

In addition to the oceanic circulation changes discussed above, there is a robust weakening of the warm water transport from the Pacific to the Indian Oceans via the ITF in the multimodel ensemble (not shown). The fractional amplitude of the ITF transport weakening is correlated with the weakening of the Walker circulation of each model, with a linear fit to the intermodel differences in the fractional change in *d*SLP explaining >50% of the intermodel differences in fractional ITF weakening. This relationship is consistent with the observed interannual variations of the ITF in relation to El Niño (La Niña) events, during which there is a reduction (enhancement) of ITF transport (e.g., Wijffels and Meyers 2004). The ITF–Walker cir-

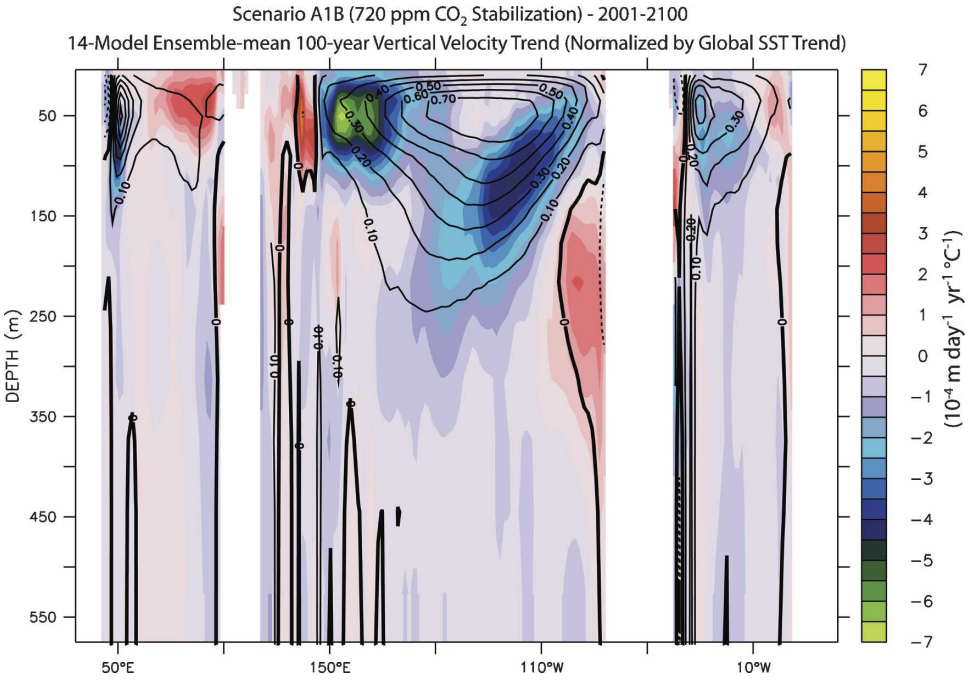

FIG. 15. Multimodel ensemble-mean tropical near-equatorial ocean vertical velocity trends forced by increased CO_2 (shading) and reference (contours). Shading shows the 14-model average of the linear least squares trend of near-equatorial (2°S–2°N average) vertical velocity over 2001–2100 of scenario A1B, with each model normalized by the global-mean surface temperature trend over the same period. Reference is the 2001–20 average, with a 0.1 m day^{-1} contour interval.

culation relationship in these models is also consistent with the mechanism proposed by Alory et al. (2007) for the observed and modeled relationship between a long-term weakening of the equatorial Pacific easterlies and the shoaling of the eastern Indian Ocean thermocline in the late twentieth century. Since large changes in the ITF can influence the character of tropical coupled variations (e.g., Song et al. 2007b), the response and impact of ITF changes to a warming climate bear examination.

4. Summary and discussion

In this study, we used climate model simulations from the IPCC AR4 archive to examine the response of the atmospheric and oceanic circulation to increasing greenhouse gases. All models simulated a weakening of the convective overturning of mass in the atmosphere as the climate warmed. This weakening was driven by the slower rate of increase of global precipitation (~2% K^{-1}) relative to the increase in lower-tropospheric water vapor (~7% K^{-1}), as described by Held and Soden (2006). The rate of increase in lower-tropospheric water vapor is well understood, and closely follows that expected from the Clausius–Clapeyron (C–C) relationship. The rate of precipitation increase was driven by changes in the surface radiation, but beyond that, the reasons for its smaller increase relative to C–C are not immediately obvious. The fact that in all models the net surface radiation (and hence global precipitation) increases more slowly than C–C suggests that physical constraints limit its rate of increase, some are discussed by Hartmann and Larson (2002), Larson and Hartmann (2003), and Held and Soden (2006). Further research on the mechanisms that determine the rate of surface radiation response to global warming would help to determine which limitations to these constraints exist.

The modeled weakening of the atmospheric convection in the Tropics occurred preferentially in the zonally asymmetric (i.e., Walker) component of the flow rather than the zonal-mean (i.e., Hadley) component. This projection is also consistent across all the models, though the reasons for this strong preference are not clear from our analysis. It may be that the zonal-mean Hadley cell is restricted by other factors, such as meridional energy transport requirements, from decreasing in strength as rapidly, whereas the Walker cell has no such constraints. Over most regions of the Tropics, the changes in the atmospheric circulation acted to oppose the background vertical motion at a rate of

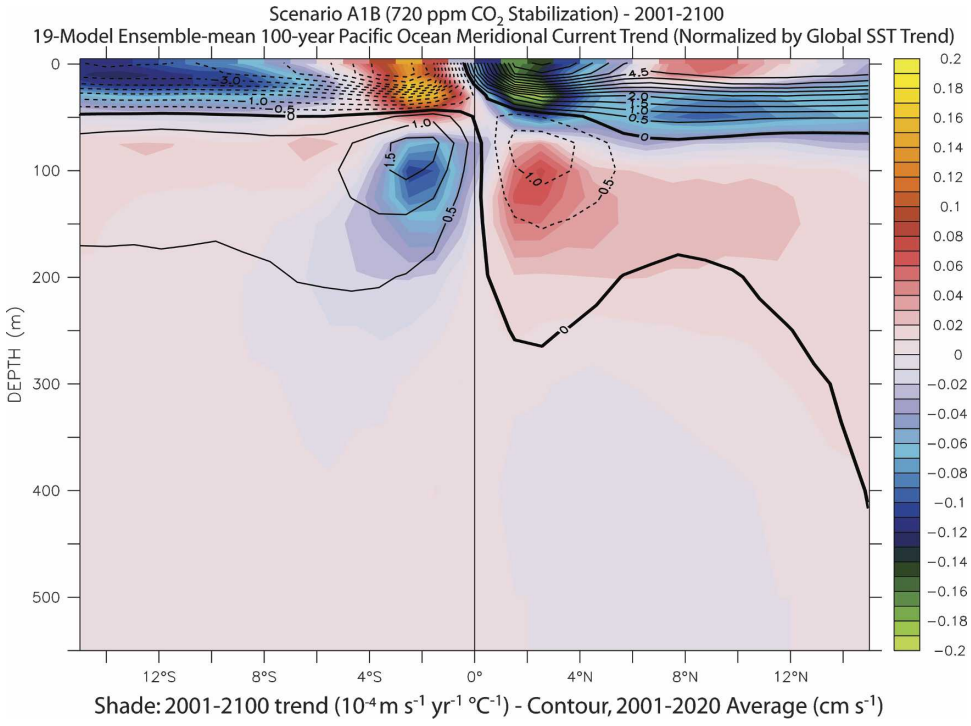

FIG. 16. Multimodel ensemble-mean tropical Pacific Ocean meridional velocity trends forced by increased CO_2 (shading) and reference (contours). Shading shows the 18-model average of the linear least squares trend of tropical Pacific (130°E–80°W average) vertical velocity over 2001–2100 of scenario A1B, with each model normalized by the global-mean surface temperature trend over the same period. Reference is the 2001–20 average, with a 0.5 cm s^{-1} contour interval.

~5%–10% K^{-1} global warming (Fig. 7). A notable exception was the central equatorial Pacific, where an eastward shift in convection acted to reinforce the ascending motions found there.

The weakened overturning may also have important implications in determining climate sensitivity. For example, the persistence of low cloud cover in the subtropics is closely tied to the strength of midtropospheric subsidence as well as lower-tropospheric stability (Klein and Hartmann 1993; Miller 1997; Clement and Seager 1999; Larson et al. 1999; Bony et al. 2004), although the response of low clouds to a reduction in midtropospheric subsidence varies considerably from model to model (Bony and Dufresne 2005). The weaker circulation may be responsible for initiating changes in low cloud cover that are currently thought to provide the largest source of uncertainty in current model estimates of climate sensitivity (Soden and Held 2006; Webb et al. 2006) and can act to reinforce El Niño–like patterns of response in coupled model simulations (Meehl and Washington 1996). In addition, the spatial structure of the weakening of midtropospheric circulation in these models has been connected to the structure of midtropospheric relative humidity changes (Vecchi and Soden 2007).

Modeled changes in both the atmospheric and ocean circulation over the tropical Pacific exhibited a spatial pattern that is suggestive of more El Niño–like conditions in a warmer climate. These included a weakening of the Walker circulation and eastward shift of convection over the central equatorial Pacific (Figs. 7–8), a reduction in SLP gradients across the equatorial Pacific (Fig. 10), a reduction in tilt of the Pacific thermocline and shoaling of the thermocline depth in the western Pacific (Fig. 12), and a preferential warming of SSTs along the eastern equatorial Pacific (Fig. 8). However, the mechanisms underlying these changes were fundamentally different from those involved in El Niño, and are present in both ocean mixed layer and full ocean dynamics coupled climate models. In fact, the weakening of the Walker circulation in response to global warming was larger in models with an ocean mixed layer model than in fully coupled climate models (Figs. 9 and 10): the net effect of ocean dynamical changes in the equatorial Pacific was to counter the thermodynamically driven weakening of the Walker circulation.

The difference between the equatorial Pacific response of the slab and fully coupled runs is consistent with the "Ocean Thermostat" mechanism of Clement et al. (1996) and Cane et al. (1997), which hypothesizes

that the coupled response to dynamical upwelling of older ocean water in the eastern Pacific leads to an increase in zonal SST gradients (and a stronger Walker circulation). Although the relevance of the Ocean Thermostat to the stabilized response of the tropical Pacific Ocean has been questioned (e.g., Liu 1998), it may still be active in this transient response of the climate models to changes in radiative forcing. Additionally, the tendency for these models to show larger warming in the equatorial oceans than the subtropical oceans (Liu et al. 2005) could act to counter the weakening of the Walker circulation, since in the subtropical regions of warming minimum are where the waters that are eventually upwelled along the equatorial Pacific are subducted (e.g., Liu 1998; Liu and Huang 1998). However, for the GCMs analyzed here, the atmospheric weakening (Betts and Ridgway 1989; Knutson and Manabe 1995; Betts 1998; Held and Soden 2006) appears to be a dominant control to the change in intensity of the Walker circulation in a warming climate. Further studies should address the extent to which the Ocean Thermostat or subduction of subtropical waters modulate changes in tropical circulation in this class of models, as well as the interplay between oceanic circulation and the thermodynamic constraints on atmospheric circulation in determining the full character of tropical atmospheric response to global warming.

The similarity between the time-mean tropical Pacific changes in the IPCC AR4 models and El Niño is not indicative of increased El Niño amplitude or frequency in a warming climate. The response of El Niño to increased CO_2 forcing in the IPCC AR4 climate models is quite model dependent (e.g., Merryfield 2006; vOPC05; Guilyardi 2006; Meehl et al. 2006); many factors influence El Niño amplitude and frequency (e.g., Wittenberg 2002; Capotondi et al. 2006; Guilyardi 2006; Wittenberg et al. 2006). We have shown that, in contrast with changes to El Niño, the tendency for a long-term weakening of the Walker circulation in response to a warming climate is a fairly robust characteristic of this class of climate models.

Many aspects of the Indian Ocean response to increased CO_2 are similar to the changes seen during an Indian Ocean Dipole–Zonal Mode (IODZM) event (e.g., Webster et al. 1999; Saji et al. 1999; Yamagata et al. 2004; Song et al. 2007a). For example, the zonal SLP gradient across the equatorial Indian Ocean weakens, there is a weakening of the zonal overturning of air in the Indian basin, there is circulation-induced increase in precipitation in the western Indian Ocean (an area that shows enhanced rainfall during positive IOD events), the eastern equatorial Indian Ocean thermocline shoals, and the equatorial currents weaken. The extent to which the IOD serves as a useful analog for understanding the monsoonal and other responses to increases in atmospheric CO_2 concentrations should be explored.

The model-projected shoaling of the eastern Indian Ocean thermocline is consistent with the observed evolution over the past 40 yr (Alory et al. 2007), and the twentieth-century simulations by the IPCC AR4 models appears to be driven by changes in radiative forcing and related to a weakening of the Pacific Walker circulation, via a reduction of the Indonesian Throughflow (ITF; Alory et al. 2007). A weakening of the ITF, as well as the Indian Ocean shallow overturning circulation, since the 1950s was documented in a recent study (Schoenefeldt and Schott 2006). Further studies are needed to understand the relationship—if any—between the changes to Indian Ocean circulation in the last 50 yr and the response of the global climate system to increased CO_2.

Many observational studies have found changes in tropical Pacific oceanic and atmospheric conditions consistent with a weakened Walker circulation over the twentieth century, including the following: an overall tendency to "El Niño–like" conditions (Trenberth and Hurrell 1994; Graham 1994; Zhang et al. 1997; Deser et al. 2004; Norris 2005), a weakening of equatorial easterlies (e.g., Harrison 1989; Clarke and Lebedev 1996), coral proxy data that indicate a tendency for lower surface salinity, warmer surface temperatures, and reduced upwelling in the central tropical Pacific (e.g., Urban et al. 2000; Cobb et al. 2001, 2003), and proxy data from deep sponges as well as instrumental data indicate a shoaling of the western equatorial Pacific thermocline (Clarke and Lebedev 1997; Moore et al. 2000; Vecchi et al. 2006). Recent studies (Zhang and Song 2006; Vecchi et al. 2006) have also found a systematic weakening of the SLP gradient across the tropical Pacific, consistent with a deceleration of the atmospheric Walker circulation. However, determining the source of multidecadal changes is complicated by the considerable internal variability to tropical Pacific climate system (e.g., Zhang et al. 1997; Deser et al. 2004; Karspeck et al. 2004; Seager et al. 2004; Vecchi et al. 2006). A recent analysis (Vecchi et al. 2006) showed that the 1861–2000 changes in SLP were inconsistent with that expected from the internal variability of all IPCC AR4 models; instead, the observed long-term SLP changes were only reproduced when the historical anthropogenic forcing was imposed on a climate model.

Meanwhile, some analyses of SST changes over the twentieth century indicate that the system has been tending toward a more La Niña–like state, with the eastern equatorial Pacific actually becoming cooler

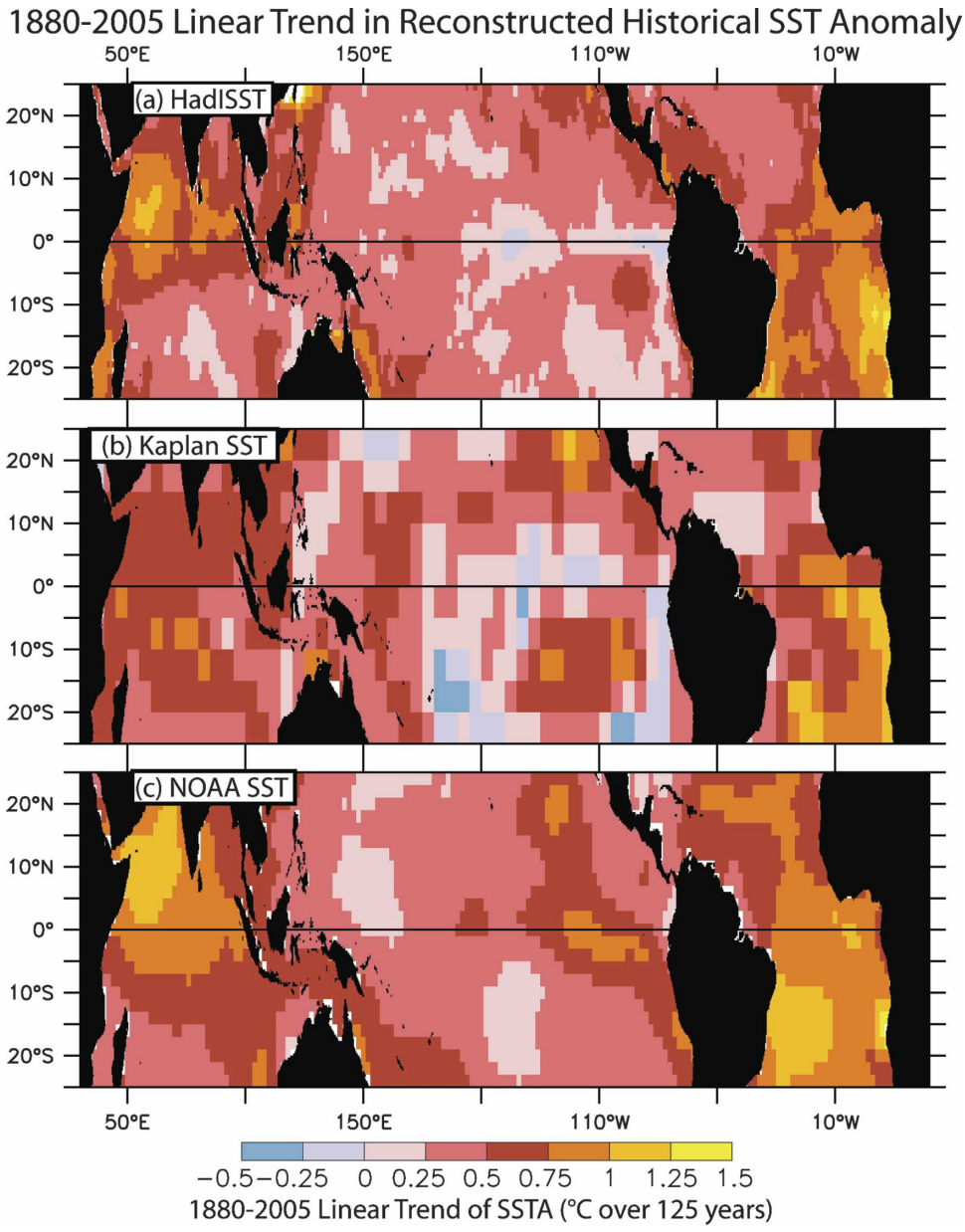

FIG. 17. Linear trend in historical SST anomaly, from two different reconstructions: (a) Hadley Centre SST (Rayner et al. 2003), (b) Kaplan et al. (1998), and (c) Smith and Reynolds (2004) products. Shading indicates the change between January 1880 and December 2005 of a linear least squares trend fit to each monthly time series at each point. Monthly mean climatology removed before computing trend. Units: °C over 125 yr.

over time (e.g., Cane et al. 1997; Hansen et al. 2006). However, different reconstructions of tropical Pacific SST over the instrumental record are inconsistent with each other: linear trends in tropical Pacific SST over the period 1880–2005 exhibit a La Niña–like structure when computed using the Kaplan (Kaplan et al. 1998) and the Hadley Centre Coupled Sea Ice and SST (HadISST; Rayner et al. 2003) reconstructions, while trends computed using the National Oceanic and Atmospheric Administration (NOAA) extended SST reconstruction (Smith and Reynolds 2004) show an El Niño–like structure (see Fig. 17). These three products differ in their analysis procedure, the corrections applied to the data before the 1940s (HadISST and Kaplan share a correction algorithm, which differs from that of the NOAA product), and data sources (e.g., the NOAA product

uses only in situ measurements over the whole record, while the source data for Kaplan and HadISST includes satellite-derived SST starting in the early 1980s; the source data for Kaplan and HadISST include additional in situ observations from the Met Office archive not present in the NOAA product). Though the overall tendency for warming is robust, there are discrepancies in the spatial structure of the changes in all three tropical basins. Until the disagreement between the various SST records is resolved, it will be difficult to understand the relationship between the observed SST and SLP records. Were the reconciliation between the various SST datasets to reveal that the SST gradient across the Pacific had been increasing over the past 125 yr, this would be inconsistent with a traditional understanding of the relationship between SST and SLP gradients and the SLP changes reported by Vecchi et al. (2006). This would force one to reevaluate either the SLP record, or the physical processes connecting SST and SLP on these multidecadal time scales.

It is likely that aspects of the observed (and future) record—even on multidecadal time scales—have been (and will be) dominated by natural variability, which may obscure radiatively forced changes. The extent to which El Niño provides a useful analog for understanding and describing the remote climate response to the tropical atmospheric slowdown in a warming climate bears examination. For example, aspects of the robust increase in tropical Atlantic vertical wind shear in this class of models in response to increase CO_2 is connected with the weakened Pacific Walker circulation (Vecchi and Soden 2007), a relation similar to the El Niño response. Also, since the CO_2-induced changes project onto many of the characteristics of El Niño, long-term changes may impact the identification of interannual El Niño events for a given reference climatology. Secular changes in the character of El Niño may be obscured by—or arise as an artifact of—radiatively forced changes tropical atmospheric circulation; conversely, the intensity and broad spectral character of unforced tropical Indo-Pacific climate variability poses a substantial challenge to identifying long-term changes in observational records.

Acknowledgments. We acknowledge the various international modeling groups for providing the data that permitted this analysis. We also acknowledge the Program for Climate Model Diagnosis and Intercomparison (PCMDI) and the IPCC Data Archive at Lawrence Livermore National Laboratory (supported by the Office of Science, U.S. Department of Energy) for collecting, archiving, and making the data readily available. This research was partially supported by a grant from the NASA NEWS program. We are grateful to two anonymous reviewers, and Amy Clement, Isaac Held, Tom Knutson, Gabriel Lau, Ants Leetmaa, Zhengyu Liu, Jian Lu, Andrew Wittenberg, Sebastian Ilcane, and Autumn Laperra for their comments and encouragement.

REFERENCES

Allen, M. R., and W. J. Ingram, 2002: Constraints on future changes in the hydrological cycle. *Nature,* **419,** 224–228.

Alory, G., S. Wijffels, and G. Meyers, 2007: Observed temperature trends in the Indian Ocean over 1960–1999 and associated mechanisms. *Geophys. Res. Lett.,* **34,** L02606, doi:10.1029/2006GL028044.

An, S.-I., and B. Wang, 2000: Interdecadal change of the structure of the ENSO mode and its impact on ENSO frequency. *J. Climate,* **13,** 2044–2055.

Betts, A. K., 1998: Climate-convection feedbacks: Some further issues. *Climatic Change,* **39,** 35–38.

——, and W. Ridgway, 1989: Climatic equilibrium of the atmospheric convective boundary layer over a tropical ocean. *J. Atmos. Sci.,* **46,** 2621–2641.

Boccaletti, G., R. C. Pacanowski, S. G. H. Philander, and A. V. Fedorov, 2004: The thermal structure of the upper ocean. *J. Phys. Oceanogr.,* **34,** 888–902.

Boer, G. J., 1993: Climate change and the regulation of the surface moisture and energy budgets. *Climate Dyn.,* **8,** 225–239.

Bony, S., and J.-L. Dufresne, 2005: Marine boundary layer clouds at the heart of tropical cloud feedback uncertainties in climate models. *Geophys. Res. Lett.,* **32,** L20806, doi:10.1029/2005GL023851.

——, ——, H. Le Treut, J.-J. Morcrette, and C. Senior, 2004: On dynamic and thermodynamic components of cloud changes. *Climate Dyn.,* **22,** 71–86.

Cane, M. A., 1979: The response of an equatorial ocean to simple wind stress patterns. II: Numerical results. *J. Mar. Res.,* **37,** 253–299.

——, and E. S. Sarachik, 1977: Forced baroclinic ocean motions. Part II: The linear equatorial bounded case. *J. Mar. Res.,* **35,** 395–432.

——, A. C. Clement, A. Kaplan, Y. Kushnir, D. Pozdnyakov, R. Seager, S. E. Zebiak, and R. Murtugudde, 1997: 20th century sea surface temperature trends. *Science,* **275,** 957–960.

Capotondi, A., A. T. Wittenberg, and S. Masina, 2006: Spatial and temporal structure of tropical Pacific interannual variability in 20th century coupled simulations. *Ocean Modell.,* **15,** 274–298.

Chou, C., and J. D. Neelin, 2004: Mechanisms of global warming impacts on regional tropical precipitation. *J. Climate,* **17,** 2688–2701.

Clarke, A. J., and A. Lebedev, 1996: Long-term changes in equatorial Pacific trade winds. *J. Climate,* **9,** 1020–1029.

——, and ——, 1997: Interannual and decadal changes in equatorial wind stress in the Atlantic, Indian, and Pacific Oceans and the eastern ocean coastal response. *J. Climate,* **10,** 1722–1729.

Clement, A., and R. Seager, 1999: Climate and the tropical oceans. *J. Climate,* **12,** 3383–3401.

——, ——, M. A. Cane, and S. E. Zebiak, 1996: An ocean dynamical thermostat. *J. Climate,* **9,** 2190–2196.

Cobb, K. M., C. D. Charles, and D. E. Hunter, 2001: A central

tropical Pacific coral demonstrates Pacific, Indian, and Atlantic decadal climate connections. *Geophys. Res. Lett.,* **28,** 2209–2212.

——, ——, H. Cheng, and R. L. Edwards, 2003: El Niño/Southern Oscillation and tropical Pacific climate during the last millennium. *Nature,* **424,** 271–276.

Collins, W. D., and Coauthors, 2006: The Community Climate System Model version 3 (CCSM3). *J. Climate,* **19,** 2122–2143.

Delworth, T. L., and Coauthors, 2006: GFDLs CM2 global coupled climate models. Part I: Formulation and simulation characteristics. *J. Climate,* **19,** 643–674.

Deser, C., A. S. Phillips, and J. W. Hurrell, 2004: Pacific interdecadal climate variability: Linkages between the Tropics and North Pacific during boreal winter since 1900. *J. Climate,* **17,** 3109–3124.

Emori, S., and S. J. Brown, 2005: Dynamic and thermodynamic changes in mean and extreme precipitation under changed climate. *Geophys. Res. Lett.,* **32,** L17706, doi:10.1029/2005GL023272.

Fedorov, A. V., P. S. Dekens, M. McCarthy, A. C. Ravelo, P. B. deMenocal, M. Barreiro, R. C. Pacanowski, and S. G. Philander, 2006: The Pliocene paradox (mechanisms for a permanent El Niño). *Science,* **312,** 1485–1489.

Furevik, T., M. Bentsen, H. Drange, I. K. T. Kindem, N. G. Kvamtsø, and A. Sorteberg, 2003: Description and evaluation of the Bergen climate model: ARPEGE coupled with MICOM. *Climate Dyn.,* **21,** 27–51.

Gordon, C., and Coauthors, 2000: The simulation of SST, sea ice extents and ocean heat transport in a version of the Hadley Centre coupled model without flux adjustments. *Climate Dyn.,* **16,** 147–168.

Gordon, H. B., and Coauthors, 2002: The CSIRO Mk3 climate system model. Tech. Rep. 60, CSIRO Atmospheric Research, Aspendale, Victoria, Australia, 134 pp.

Graham, N. E., 1994: Decadal-scale climate variability in the tropical and North Pacific during the 1970s and 1980s: Observations and model results. *Climate Dyn.,* **10** (3), 135–162.

Guilyardi, E., 2006: El Niño-mean state-seasonal cycle interactions in a multi-model ensemble. *Climate Dyn.,* **26,** 329–348.

Hansen, J., M. Sato, R. Ruedy, K. Lo, D. W. Lea, and M. Medinaelizade, 2006: Global temperature change. *Proc. Natl. Acad. Sci. USA,* **103,** 14 288–14 293.

Harrison, D. E., 1989: Post World War II trends in tropical Pacific surface trades. *J. Climate,* **2,** 1561–1563.

——, and G. A. Vecchi, 2001: El Niño and La Niña: Equatorial Pacific surface temperature and thermocline variability, 1986-98. *Geophys. Res. Lett.,* **28,** 1051–1054.

Hartmann, D. L., and K. Larson, 2002: An important constraint on tropical cloud–climate feedback. *Geophys. Res. Lett.,* **29,** 1951, doi:10.1029/2002GL015835.

Hasumi, H., and S. Emori, Eds., 2004: K-1 coupled model (MIROC) description. K-1 Tech. Rep. 1, Center for Climate System Research, University of Tokyo, 34 pp.

Held, I. M., and B. J. Soden, 2006: Robust responses of the hydrological cycle to global warming. *J. Climate,* **19,** 5686–5699.

Jin, F.-F., 1997: An equatorial ocean recharge paradigm for ENSO. Part I: Conceptual model. *J. Atmos. Sci.,* **54,** 811–829.

Johns, T., and Coauthors, 2004: HadGEM1—Model description and analysis of preliminary experiments for the IPCC Fourth Assessment Report. Tech Rep. 55, Met Office, Exeter, United Kingdom.

Jungclaus, J., and Coauthors, 2006: Ocean circulation and tropical variability in the coupled model ECHAM5/MPI-OM. *J. Climate,* **19,** 3952–3972.

Kaplan, A., M. A. Cane, Y. Kushnir, A. C. Clement, M. B. Blumenthal, and B. Rajagopalan, 1998: Analyses of global sea surface temperature 1856–1991. *J. Geophys. Res.,* **103** (C9), 18 567–18 589.

Karspeck, A. R., R. Seager, and M. A. Cane, 2004: Predictability of tropical Pacific decadal variability in an intermediate model. *J. Climate,* **17,** 2842–2850.

Kim, S.-J., G. M. Flato, G. J. de Boer, and N. A. McFarlane, 2002: A coupled climate model simulation of the Last Glacial Maximum. Part I: Transient multi-decadal response. *Climate Dyn.,* **19,** 515–537.

Kirtman, B., 1997: Oceanic Rossby wave dynamics and the ENSO period in a coupled model. *J. Climate,* **10,** 1690–1704.

Klein, S. A., and D. L. Hartmann, 1993: The seasonal cycle of low stratiform clouds. *J. Climate,* **6,** 1587–1606.

Knutson, T. R., and S. Manabe, 1995: Time-mean response over the tropical Pacific to increased CO_2 in a coupled ocean–atmosphere model. *J. Climate,* **8,** 2181–2199.

Larson, K., and D. L. Hartmann, 2003: Interactions among cloud, water vapor, radiation, and large-scale circulation in the tropical climate. Part I: Sensitivity to uniform sea surface temperature changes. *J. Climate,* **16,** 1425–1440.

——, ——, and S. A. Klein, 1999: The role of clouds, water vapor, circulation, and boundary layer structure in the sensitivity of the tropical climate. *J. Climate,* **12,** 2359–2374.

Lindzen, R. S., 1990: Some coolness concerning global warming. *Bull. Amer. Meteor. Soc.,* **71,** 288–299.

Liu, Z., 1998: On the role of ocean in the transient response of tropical climatology to global warming. *J. Climate,* **11,** 864–875.

——, and B. Huang, 1998: Why is there a tritium maximum in the central equatorial Pacific thermocline? *J. Phys. Oceanogr.,* **28,** 1527–1533.

——, S. Varvus, F. He, N. Wen, and Y. Zhong, 2005: Rethinking tropical oceanic response to global warming: The enhanced equatorial warming. *J. Climate,* **18,** 4684–4700.

Lu, J., G. A. Vecchi, and T. Reichler, 2007: Expansion of the Hadley cell under global warming. *Geophys. Res. Lett.,* **34,** L06805, doi:10.1029/2006GL028443.

Lucarini, L., and G. L. Russell, 2002: Comparison of mean climate trends in the northern hemisphere between National Centers for Environmental Prediction and two atmosphere-ocean model forced runs. *J. Geophys. Res.,* **107,** 4269, doi:10.1029/2001JD001247.

Marti, O., and Coauthors, 2005: The new IPSL climate system model: IPSL-CM4. Tech. Rep., Institut Pierre Simon Laplace des Sciences de l'Environment Global, IPSL, Case 101, Paris, France.

McPhaden, M. J., 1993: TOGA-TAO and the 1991–93 El Niño-Southern Oscillation event. *Oceanography,* **6,** 36–44.

——, 1999: Genesis and evolution of the 1997–98 El Niño. *Science,* **283,** 950–954.

——, and D. Zhang, 2002: Slowdown of the meridional overturning circulation in the upper Pacific Ocean. *Nature,* **415,** 603–608.

——, and ——, 2004: Pacific Ocean circulation rebounds. *Geophys. Res. Lett.,* **31,** L18301, doi:10.1029/2004GL020727.

Meehl, G. A., and W. M. Washington, 1996: El Niño-like climate change in a model with increased atmospheric CO_2 concentrations. *Nature,* **382,** 56–60.

——, H. Teng, and G. Branstator, 2006: Future changes of El

Niño in two global coupled climate models. *Climate Dyn.,* **26,** 549–566.

Merryfield, W. J., 2006: Changes to ENSO under CO_2 doubling in a multimodel ensemble. *J. Climate,* **19,** 4009–4027.

Miller, R. L., 1997: Tropical thermostats and low cloud cover. *J. Climate,* **10,** 409–440.

Min, S.-K., S. Legutke, A. Hense, and W.-T. Kwon, 2005: Internal variability in a 1000-yr control simulation with the coupled model ECHO-G-I: Near-surface temperature, precipitation and mean sea level pressure. *Tellus,* **57A,** 605–621.

Moore, M. D., C. D. Charles, J. L. Rubenstone, and R. G. Fairbanks, 2000: U/Th-dated sclerosponges from the Indonesian Seaway record subsurface adjustments to west Pacific winds. *Paleoceanography,* **15,** 404–416.

Norris, J. R., 2005: Trends in upper-level cloud cover and surface wind divergence over the tropical Indo-Pacific Ocean between 1952 and 1997. *J. Geophys. Res.,* **110,** D21110, doi:10.1029/2005JD006183.

Philander, S. G. H., 1981: The response of equatorial oceans to a relaxation of the trade winds. *J. Phys. Oceanogr.,* **11,** 176–189.

Rayner, N. A., D. E. Parker, E. B. Horton, C. K. Folland, L. V. Alexander, D. P. Rowell, E. C. Kent, and A. Kaplan, 2003: Global analyses of sea surface temperature, sea ice, and night marine air temperature since the late nineteenth century. *J. Geophys. Res.,* **108,** 4407, doi:10.1029/2002JD002670.

Saji, N. H., B. N. Goswami, P. N. Vinayachandran, and T. Yamagata, 1999: A dipole mode in the tropical Indian Ocean. *Nature,* **401,** 360–363.

Salas y Mélia, D., and Coauthors, 2006: Description and validation of the CNRM-CM3 global coupled model. *Climate Dyn.,* in press.

Schmidt, G. A., and Coauthors, 2006: Present-day atmospheric simulations using GISS ModelE: Comparison to in situ, satellite, and reanalysis data. *J. Climate,* **19,** 153–192.

Schoenefeldt, R., and F. A. Schott, 2006: Decadal variability of the Indian Ocean cross-equatorial exchange in SODA. *Geophys. Res. Lett.,* **33,** L08602, doi:10.1029/2006GL025891.

Seager, R., A. R. Karspeck, M. A. Cane, Y. Kushnir, A. Giannini, A. Kaplan, B. Kerman, and J. Velez, 2004: Predicting Pacific decadal variability. *Earth Climate: The Ocean–Atmosphere Interaction, Geophys. Monogr.,* Vol. 147, Amer. Geophys. Union, 105–120.

Smith, T. M., and R. W. Reynolds, 2004: Improved extended reconstruction of SST (1854–1997). *J. Climate,* **17,** 2466–2477.

Soden, B. J., 2000: The sensitivity of the tropical hydrological cycle to ENSO. *J. Climate,* **13,** 538–549.

——, and I. M. Held, 2006: An assessment of climate feedbacks in coupled ocean–atmosphere models. *J. Climate,* **19,** 3354–3360.

——, D. L. Jackson, V. Ramaswamy, D. Schwarzkopf, and X. Huang, 2005: The radiative signature upper tropospheric moistening. *Science,* **310,** 841–844.

Song, Q. N., G. A. Vecchi, and A. Rosati, 2007a: Indian Ocean variability in the GFDL Coupled Climate Model. *J. Climate,* **20,** 2895–2916.

——, ——, and ——, 2007b: The role of the Indonesian Throughflow in the Indo–Pacific climate variability in the GFDL Coupled Climate Model. *J. Climate,* **20,** 2434–2451.

Tanaka, H. L., N. Ishizaki, and A. Kitoh, 2004: Trend and interannual variability of Walker, monsoon and Hadley circulations defined by velocity potential in the upper troposphere. *Tellus,* **56A,** 250–269.

Trenberth, K. E., and J. W. Hurrell, 1994: Decadal atmosphere–ocean variations in the Pacific. *Climate Dyn.,* **9,** 303–319.

——, J. Fasullo, and L. Smith, 2005: Trends and variability in column integrated atmospheric water vapor. *Climate Dyn.,* **24,** 741–758.

Urban, F. E., J. E. Cole, and J. T. Overpeck, 2000: Influence of mean climate change on climate variability from a 155-year tropical Pacific coral record. *Nature,* **407,** 989–993.

van Oldenborgh, G. J., S. Y. Philip, and M. Collins, 2005: El Niño in a changing climate: A multi-model study. *Ocean Sci.,* **1,** 81–95.

Vecchi, G. A., and B. J. Soden, 2007: Increased tropical Atlantic wind shear in model projections of global warming. *Geophys. Res. Lett.,* **34,** L08702, doi:10.1029/2006GL028905.

——, ——, A. T. Wittenberg, I. M. Held, A. Leetmaa, and M. J. Harrison, 2006: Weakening of tropical Pacific atmospheric circulation due to anthropogenic forcing. *Nature,* **441,** 73–76.

Volodin, E. M., and N. A. Diansky, 2004: El Niño reproduction in coupled general circulation model. *Russ. Meteor. Hydrol.,* **12,** 5–14.

Walker, G. T., and E. W. Bliss, 1932: World Weather V. *Memo. Roy. Meteor. Soc.,* **4** (36), 53–84.

——, and ——, 1937: World Weather VI. *Memo. Roy. Meteor. Soc.,* **4** (39), 119–139.

Wang, C., and J. Picaut, 2004: Understanding ENSO Physics—A review. *Earth Climate: The Ocean–Atmosphere Interaction, Geophys. Monogr.*, Vol. 147, Amer. Geophys. Union, 21–48.

Washington, W. M., and Coauthors, 2000: Parallel climate model (PCM) control and transient simulations. *Climate Dyn.,* **16,** 755–774.

Webb, M. J., and Coauthors, 2006: On the contribution of local feedback mechanisms to the range of climate sensitivity in two GCM ensembles. *Climate Dyn.,* **27,** 17–38.

Webster, P. J., A. M. Moore, J. P. Loschnigg, and R. R. Leben, 1999: Coupled ocean–atmosphere dynamics in the Indian Ocean during 1997-98. *Nature,* **401,** 356–360.

Wentz, F. J., and M. Schabel, 2000: Precise climate monitoring using complementary satellite data sets. *Nature,* **403,** 414–416.

Wijffels, S., and G. Meyers, 2004: An intersection of oceanic waveguides: Variability in the Indonesian Throughflow region. *J. Phys. Oceanogr.,* **34,** 1232–1253.

Wittenberg, A. T., 2002: ENSO response to altered climates. Ph.D. thesis, Princeton University, 475 pp.

——, A. Rosati, N.-C. Lau, and J. J. Ploshay, 2006: GFDL's CM2 global coupled climate models. Part III: Tropical Pacific climate and ENSO. *J. Climate,* **19,** 698–722.

Wyrtki, K., 1975: El Niño—The dynamic response of the equatorial Pacific Ocean to atmospheric forcing. *J. Phys. Oceanogr.,* **5,** 572–584.

Yamagata, T., S. K. Behera, J.-J. Luo, S. Masson, M. R. Jury, and S. A. Rao, 2004: Coupled ocean-atmosphere variability in the tropical Indian Ocean. *Earth Climate: The Ocean–Atmosphere Interaction, Geophys. Monogr.,* Vol. 147, Amer. Geophys. Union, 189–211.

Yu, Y., X. Zhang, and Y. Guo, 2004: Global coupled ocean-atmosphere general circulation models in LASG/IAP. *Adv. Atmos. Sci.,* **21,** 444–455.

Yukimoto, S., and A. Noda, 2002: Improvements in the Meteorological Research Institute Global Ocean-Atmosphere Coupled GCM (MRI-CGCM2) and its climate sensitivity. Tech. Rep. 10, NIES, Japan, 8 pp.

Zebiak, S. E., and M. A. Cane, 1987: A model El Niño–Southerrn Oscillation. *Mon. Wea. Rev.,* **115,** 2262–2278.

Zelle, H., G. Appeldoorn, G. Burgers, and G. J. van Oldenborgh, 2004: The relationship between sea surface temperature and thermocline depth in the eastern equatorial Pacific. *J. Phys. Oceanogr.,* **34,** 643–655.

Zhang, D., and M. J. McPhaden, 2006: Decadal variability of the shallow Pacific meridional overturning circulation: Relation to tropical sea surface temperatures in observations and climate change models. *Ocean Modell.,* **15,** 250–273.

Zhang, M., and H. Song, 2006: Evidence of deceleration of atmospheric vertical overturning circulation over the tropical Pacific. *Geophys. Res. Lett.,* **33,** L12701, doi:10.1029/2006GL025942.

Zhang, Y., J. M. Wallace, and D. S. Battisti, 1997: ENSO-like interdecadal variability: 1900–93. *J. Climate,* **10,** 1004–1020.